Università degli Studi di Napoli "Federico II"

Scuola Politecnica e delle Scienze di Base
Area Didattica di Scienze Matematiche Fisiche e Naturali

Dipartimento di Fisica

Master's Degree in Physics

The quest for cosmic strings: astrophysical methods

Supervisors:
Prof. Olga S. Sazhina
Prof. Massimo Capaccioli
Prof. Maurizio Paolillo
Co-supervisor:
Prof. Ester Piedipalumbo

Candidate:
Diana Scognamiglio
Matricola N94/329

A.Y. 2016/2017

To these intense years,
to mum and dad, my strength,
to M., always by my side.

“The absence of evidence is not the evidence of absence.”
Carl Sagan

Abstract

The seed of my thesis was planted in 2013 within the project "Messaggeri della Conoscenza" when I spent one month in Moscow and in Dubna and started a scientific collaboration with the Moscow State University (MSU).

My thesis work focuses on the study of Cosmic Strings (CS). The existence of cosmic strings was first proposed by Thomas Kibble in 1976 [5], who drew on the theory of line vortices in superconductors to predict the formation of similar structures in the universe, at large as it and cooled during the early phases of the Big Bang. They are hypothetical remnants of the early universe whose formation is a predicted result of spontaneous symmetry breaking. Being relics of the phase transitions that produced them, if they are stable and survive for a significant amount of time, they may leave an imprint on many astrophysical and cosmological observables. In this way, Cosmic Strings provide us with the possibility to understand fundamental physical processes, offering us a unique window on the early universe that would otherwise be inaccessible to us.

To understand the cosmological context and the effect of cosmic strings I start, in Chapter 1, with a summary of basic cosmological concepts that will be helpful to understand cosmic strings as topological defects. In Chapter 2, I describe the processes leading to the formation of topological defects and cosmic strings models; Chapter 3 is a survey on different types of defects, with very different characteristics and dimensions. A CS produces a peculiar conical topology of the space-time and it may cause detectable effects both in radio and in optical data. The main part of my work thesis, described in Chapter 4, deals with the developement of an effective strategy to detect and characterize these elusive physical entities. Our procedure is a mix of two methods for CS search: the analysis of the anisotropy of the CMB radiation and the detection of the strong gravitational lensing effects of remote sources

by a CS. Radio maps of CMB anisotropy, provided by the space mission Planck for various frequencies, were filtered and then processed through convolution with modified Haar functions (MHF) to search for CMB gradients induced by a CS. This procedure shows that strings can only be semilocal, with the upper restriction on individual string tension (linear density) of $G\mu/c^2 \leq 7.36 \times 10^{-7}$. The result was a list of preliminary CS candidates with the amplitude $\delta T/T \lesssim 40\mu K$. We select the best one (Cosmic String candidate No. 1 = CSc-1) and on it we carry on an independent optical analysis, based on the search of gravitationally lensed sources. First, we verified the feasibility of our experiment: the test gives successful results demonstrating that, using our data, is possible to detected the presence of cosmic strings at $> 2.6\sigma$ confidence level. Using photometric criteria, with both an automatic algorithm and through visual inspection, we identify some pairs of lensed galaxies, in order to look for a convincing excess over the average density of background galaxy pairs in ordinary fields. We find an excess of 20% of pairs in string fields respect to the number of pairs in the ordinary fields.

We analyze the possibility to find a preferred orientation of the pairs for different value of the separation between pair components. The result is that we find an excess: there is a dominant direction of the arrangement of pairs for $[8'', 9'']$ angular separations. Then we plot, separately for each separation interval, the number of pairs of different intervals of inclination angle β, achieving a significant excess of $[4'', 6'']$ distanced pairs in the interval $\beta \in [20°, 30°]$. Both Student's test and Poisson's distribution of the pairs in each angle bin, confirm this result.

For the $[4'', 6'']$ distanced pairs, we also find that the orientation between the pairs and the hypothetical string direction is almost orthogonal in the sky: this is consistent with the hypothesis that some of these sources are lensed by a CS.

Even if no definitive conclusion can be drawn at this point, we thus found some observational signatures expected from Cosmic Strings, using for the first time two indipendent methods in combination. The definitive confirmation of the gravitational lensing origin of our pairs candidates requires spectroscopic observations. We plan to acquire their spectra as well as to continue the study of the spectral and morphological features of the lens candidates in the CSc-1 fields.

Contents

Chapter 1

Introduction to modern cosmology

According to our current knowledge, the universe originated 13.7×10^9 years ago. Its evolution from one hundredth of a second up to the present day can be reliably described by the **Big Bang model**. This includes the expansion of the universe, the origin of light elements and the relic radiation from the initial fireball, as well as a framework for understanding the formation of galaxies, other large-scale structures and exotic objects such as example primordial black holes, cosmological strings, textures, etc. The Big Bang model is now so well tested that it is known as the **Standard Cosmological model**. Such model is based upon the so called cosmological principle [1], which asserts that the universe is, on large scales, both homogeneous and isotropic. This assumption is supported by many evidences including the measured distributions of galaxies and of faint radio sources, but by far the best evidence comes from the observed uniformity of the cosmic microwave background radiation on large angular scales. However, on smaller scales this assumption is not true, so the question arise of what is the origin of the density fluctuations that produced the observed anisotropies and ultimately led to the formation of galaxies and other large scale structures. In this scenario, **Cosmic Strings** (**CS**) are the first candidates as the sources of the density perturbations that cause the formation of structures in the universe. Recent studies have indicated that, cosmic strings could still be partly responsible for these perturbations [2] and Inflation theory gives a explanation for the current data.

To understand the role of the cosmic strings in a cosmological context, we start in this section with a summary of basic cosmology concepts.

1.1 The model and formalism

Since the early universe is homogeneous on large scales, the metric that includes the assumptions of the homogeneity and the isotropy of space-time most suitable for the study of cosmology is the Friedmann-Robertson- Walker (**FRW**) metric:

$$ds^2 = dt^2 - a^2\left(t\right)dl^2 \tag{1.1}$$

where t is the cosmological time, dl represents the line element on a three-dimensional space of constant curvature, and $a\left(t\right)$ is the scale factor that determines the fractional or Hubble expansion rate:

$$H\left(t\right) = \frac{\dot{a}\left(t\right)}{a\left(t\right)} \tag{1.2}$$

The scale factor $a\left(t\right)$ is the only degree of freedom to consider following the (strong) demand of the cosmological principle and it contains informations on the dynamics of the universe on a large scale. In spherical coordinates, this metric takes the form:

$$dl^2 = \frac{dr^2}{1-kr^2} + r^2\left(d\theta^2 + \sin\theta d\phi^2\right) \tag{1.3}$$

where the constant curvature k is determined by the spatial topology and geometry of the universe and can be > 0, < 0 or $= 0$ if the universe is, respectively, closed, open or flat.

The physical distances between objects are determined introducing the comoving distances and multiplying them by the scale factor $a\left(t\right)$; in addition, it is often useful to introduce an alternative time coordinate, the conformal time τ , defined as $d\tau = dt/a\left(t\right)$, leading to the metric

$$ds^2 = a^2\left(\tau\right)\left[d\tau^2 - dl^2\right]. \tag{1.4}$$

Once the cosmological principle has been assumed, the Friedmann equations are:

$$3\frac{\dot{a}^2 + k}{a^2} = 8\pi G\epsilon \tag{1.5}$$

$$\dot{\epsilon} = -3\frac{\dot{a}}{a}\left(\epsilon + p\right) \tag{1.6}$$

where ϵ is the energy density, p is the pressure and G the universal gravitational constant. They allow to derive the evolution of the universe (i.e. $a\left(t\right)$) given a certain state equation $p = p\left(\epsilon\right)$ for the cosmic fluid.

The age of the universe is currently estimated to be about 13.7 billion years [3], [4]. The primordial universe was very hot and dense and was cooled by the expansion, with the temperature decreasing as $T(t) \backsim a(t)^{-1}$. The Hubble expansion rate is determined by the energy contents of the universe. In a universe dominated by *radiation* or very *relativistic matter* (the hottest, earliest stages), the scale factor evolves as $a(t) \backsim t^{1/2}$ and the energy density in radiation as $\rho_{radiation} \sim a(t)^{-4} \sim t^{-2}$. The energy density of non-relativistic matter is inversely proportional to volume $\rho_{matter} \sim a(t)^{-3}$ and eventually takes over (after about 4000 years), leading to a period of matter domination, during which $a(t)^{2/3}$ and therefore $\rho_{matter} \sim t^{-2}$. More recently – about five billion years ago – we have entered a second epoch of accelerated expansion due possibly to a cosmological constant or some unknown form of *dark energy* whose energy density is maybe constant in time $\rho_{dark\ energy} \sim const$. The current cosmological model accepts that the energy density in the universe today would be dominated by dark energy (about 74%), followed by about 22% dark matter and only about 4% of regular (baryonic) matter [10]. Fig. 1.1 below briefly summarizes the thermal history of the universe as it is currently understood.

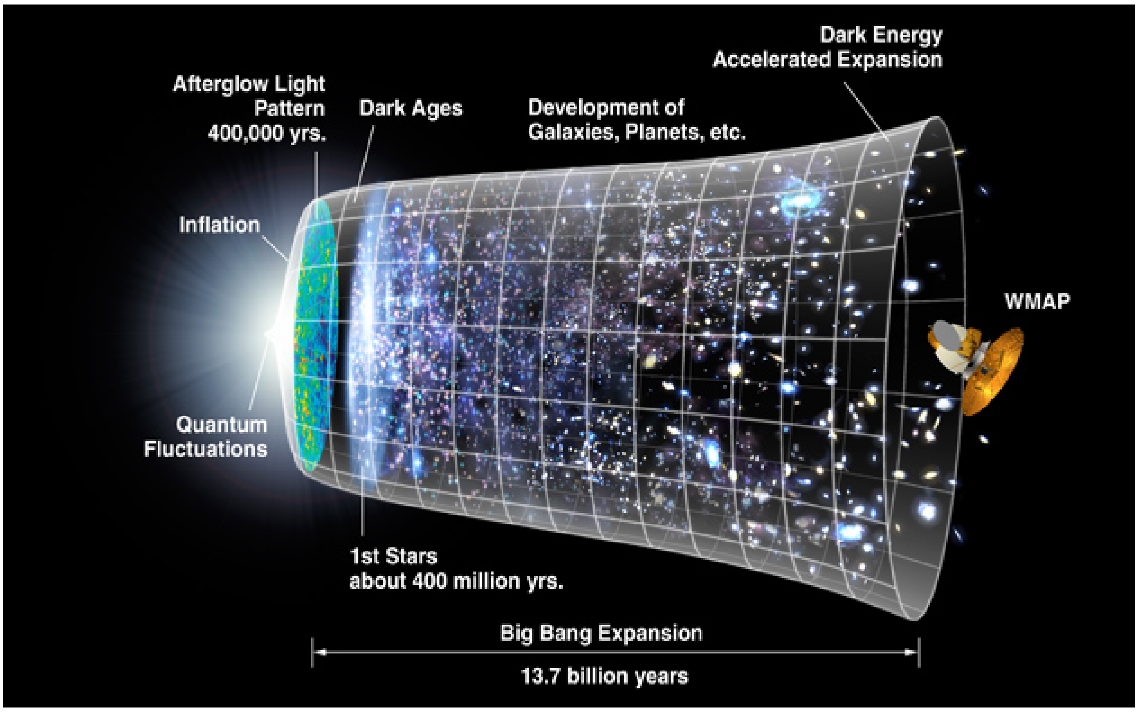

Figure 1.1: Diagram of evolution of the universe from the Big Bang (left) - to the present (right).

The Standard Cosmological model, that uses the (FRW) metric, is able to explain several features which characterize the evolution of universe: (i) the expansion of the universe, (ii) the origin of the cosmic background radiation, (iii) the nucleosynthesis of elements, and (iv) the formation of large-scale structures. However, there are some questions, related mainly to the initial conditions, to which the Hot Big Bang model has been so far unable to provide correct answers. It is possible to find an explanation introducing the idea of inflation. Inflation essentially consists of a phase of accelerated expansion, corresponding to forces of negative pressure (or, equivalentely positive tension), which counteracts the gravitational forces and an equation of state $3p < -\rho$, which took place at a very high energy scale. From the observational point of view, the uniformity of the CMB indicates that at the epoch of last scattering the universe was isotropic and homogeneous, with a high degree of precision 10^{-5}. At very large scale, universe is homogeneous, while at small scales today we observe large inhomogeneities. The two main models suggest that the initial density perturbations can either be due to freezing in of quantum fluctuations of a scalar field during an inflationary period, or they may be seeded by a class of topological defects, which could have formed naturally during a symmetry breaking phase transition in the early universe. It is this last model that we will analyze in the next chapter.

Chapter 2

Topological defects formation: the phase transitions

Phase transitions are physical phenomena: the changes of phase of the substances from solid to liquid (e.g. ice to water) and liquid to gas (e.g. water to steam) are few examples of the phase transitions that occur in our daily life. Consider a cold day: ice forms quickly on the surface of a pond. However, it does not grow as a smooth, featureless covering. Instead, the water begins to freeze in many places independently, and the growing plates of ice join up in random way, leaving zig-zag boundaries between them. These irregular margins are an example of what physicists called **topological defects**. "Defects" because they are places where the crystal structure of the ice is disrupted and "topological" because an accurate description of them involves ideas of symmetry embodied in topology, the branch of mathematics that focuses on the study of continuous surfaces. Current theories of particle physics likewise predict that a variety of topological defects would almost certainly have formed during the early evolution of the universe. Just as water turns to ice (a phase transition) when the temperature drops, so the interactions between elementary particles run through distinct phases as the typical energy of those particles falls with the expansion of the universe. When conditions favour the appearance of a new phase, it generally crops up in many places at the same time, and when separated regions of the new phase run into each other, topological defects are the result.

An important category of phase transitions is that which corresponds to Spontaneous Symmetry Breaking **(SSB)** and one such example is the phase transition from paramagnetic phase to ferromagnetic phase. Most of the phase transitions are associated with a change in symmetry of the system.

However, it is not essential that the symmetry of the system changes in the phase transition. Also, the universe underwent several phase transitions as it became cooler.

In this chapter, we will describe various properties of the phase transitions in the early universe (Grand Unification Theory (GUT), Electroweak and Quantum Chromodynamics (QCD)) and the formation of topological defects as result of spontaneous symmetry breaking phase transitions.

2.1 The spontaneous symmetry breaking

One of the most important concepts in modern particle physics is that of spontaneous symmetry breaking. The idea that there are underlying symmetries of nature that are not manifest at ground level (i.e. the vacuum) appears to play a crucial role in the unification of the forces. In all unified gauge theories, including the standard model of particle physics, the underlying gauge symmetry is larger than that of vacuum. In the early universe, GUT unifies strong and electroweak interactions and the electroweak theory, a local gauge theory combines electromagnetic and weak interactions and it is based on the idea of SSB. The phenomenon of SSB is most often implemented with a scalar field, called Higgs field in the context of particle physics. Due to the spontaneous symmetry breaking of electroweak symmetry, the fundamental gauge bosons i.e. W^+, W^- and Z^0 become massive: this is the famous Higgs mechanism. In unified gauge theories, the symmetry of the Lagrangian is broken spontaneously during a phase transition. The effective potential, which is the expression of free energy for the fields in the Lagrangian taking into account all quantum corrections, contains all the information about the phases of the system as well as the order of the phase transition. In this section, we will describe basic physics of SSB. The metric used in this work has signatures $(+,-,-,-)$ [6].

The essential features of SSB can be illustrated in the following example, first studied by Goldstone. Let us consider the Lagrangian density:

$$\mathfrak{L} = \left(\partial_\mu \overline{\phi}\right)\left(\partial^\mu \phi\right) - V\left(\phi\right) \tag{2.1}$$

where ϕ is a complex scalar field and the potential $V(\phi)$ is given by

$$V\left(\phi\right) = \frac{1}{4}\lambda\left(\overline{\phi}\phi - \eta^2\right)^2. \tag{2.2}$$

The positive real constants λ and η are, respectively, the self-interaction term, that states how strongly two scalar particles interact, and the mass term. That potential is also known as the Mexican hat potential, Fig. 2.1.

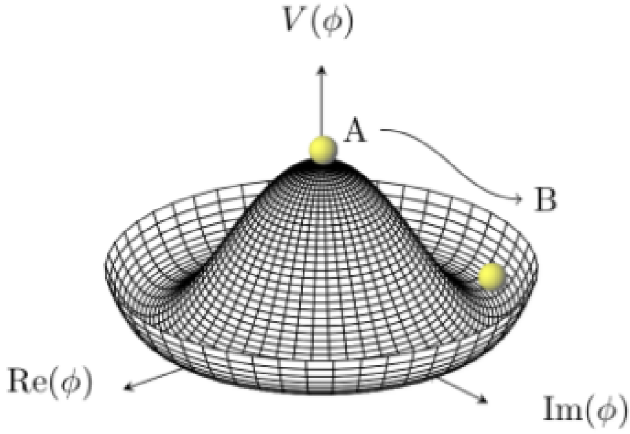

Figure 2.1: Mexican hat potential.

The Lagrangian has a rotational symmetry. This means that under (circular) transformations in the ϕ,ϕ^* plane the Lagrangian does not change. Just by looking at Fig. 2.1 it can be seen that the potential is invariant under the group $U(1)$ of global phase transformations,

$$\phi(x) \to e^{i\alpha}\phi(x)\,. \tag{2.3}$$

Here, "global" indicates that α is independent of the space-time location x. The minima of the potential $V(\phi)$ lie on the circle $|\phi| = \eta$ and this circle represents the vacuum manifold of the theory. The ground state (the vacuum) of the theory is characterized by a non-zero expectation value of the field operator ϕ

$$\langle 0 |\phi| 0\rangle = \eta e^{i\theta} \tag{2.4}$$

with an arbitrary phase θ. The phase transformation (2.3) changes θ into $\theta + \alpha$. Hence, the vacuum state $|0\rangle$ is not invariant under (2.3), and the symmetry is spontaneously broken. The state of unbroken symmetry with $\langle 0 |\phi| 0\rangle = 0$ corresponds to a local maximum of $V(\phi)$. Due to the SSB of a continuous global symmetry, massless Goldstone bosons appear in the theory. This can be seen as follows. In order to study the particle spectrum in this model, we have to consider small perturbations of the field around that state. They are described by the Lagrangian (2.1) with

$$V(\phi) \approx -\frac{1}{2}\eta^2\bar{\phi}\phi + const \tag{2.5}$$

The negative sign of the mass term in (2.5) indicates the instability of the symmetry state. The broken symmetry vacua with different values of θ are all equivalent, and their properties can be found by studying any one of them. Choosing the vacuum with $\theta = 0$, we can represent ϕ as

$$\phi = \eta + \frac{1}{\sqrt{2}} (\phi_1 + i\phi_2) \tag{2.6}$$

where ϕ_1 and ϕ_2 are real fields with zero vacuum expectation values. Substitution of (2.6) into the Lagrangian (2.1) gives

$$\mathfrak{L} = \frac{1}{2} (\partial_\mu \phi_1)^2 + \frac{1}{2} (\partial_\mu \phi_2)^2 - \frac{1}{2} \lambda \eta^2 \phi_1^2 + \mathfrak{L}_{\mathsf{int}} \tag{2.7}$$

where the interaction term $\mathfrak{L}_{\mathsf{int}}$ includes cubic and high-order terms in ϕ_1 and ϕ_2. The above form of the Lagrangian shows that the field ϕ_1 corresponds to a massive particle with positive mass, $\mu = \sqrt{\lambda}\eta$, while the field ϕ_2 becomes massless. The reason for this is clear from Fig. 2.1: ϕ_1 corresponds to radial oscillations about a point on the circle of minima, $|\phi| = \eta$, while ϕ_2 corresponds to motion around the circle. The appearance of massless scalar particles, called Goldstone boson, is a general feature of spontaneously broken global symmetries. Despite of its simplicity, this model captures the essential physics of SSB. In general, the number of Goldstone bosons will be equal to the dimension of the vacuum manifold (number of broken generators). In a phenomenological model, a well-known example of Goldstone bosons are pions, which appear as a consequence of SSB of chiral symmetry in QCD in the massless limit of quarks. If the same argumentation indeed is applied to the real fields, φ and θ, the Lagrangian becomes

$$\mathfrak{L} = \frac{1}{2} (\partial_\mu \varphi)^2 + \eta^2 (\partial_\mu \theta)^2 - \frac{1}{2} \lambda \eta^2 \varphi^2 + \mathfrak{L}_{\mathsf{int}} \tag{2.8}$$

with φ the massive scalar particle and θ the massless Goldstone particle. It should be pointed out, however, that with an opportune gauge it is possible to eliminate the above-cited boson.

For a straight, static string, it is sufficient to look for a solution of the equations of motion in two spatial dimensions, and then to use translation invariance to extend the solution to three dimensions. For example, if the solution in two dimensions is $\phi_0(x, y)$, then the solution in three dimensions is $\phi(x, y, z) = \phi_0(x, y)$. The static string solution obtained using the Lagrangian (2.1) is:

$$\phi(x, y) = \eta f(m\rho) e^{in\theta} \tag{2.9}$$

where (ρ, θ) are polar coordinates on the xy-plane, $m^2 = \lambda\eta^2$, and n is the (integer) winding number of the string. This string solution is known as a **"global"** string because there are no gauge fields in the model.

2.2 Kibble mechanism

As we know, for temperatures much larger than the critical one the vacuum expectation value of the scalar field vanishes at all points of space, whereas for $T < T_c$ it evolves smoothly in time towards a non vanishing $\langle|\phi|\rangle$ [6]. However, the new value of $\langle|\phi|\rangle$ is not uniform in space due to both thermal and quantum fluctuations. This leads to the existence of domains wherein the $\langle|\phi(\overrightarrow{x})|\rangle$ is coherent and regions where it is not. In each domain, the configuration of the order parameter field can be taken as nearly uniform while it varies randomly from one domain to another.
In a first-order phase transition, at very high energies the symmetry breaking potential has $\langle|\phi|\rangle = 0$ as the only vacuum state. When the temperature goes down to T_c, a set of degenereted vacua develops and the transition is not smooth as before, for a potential barrier separates the old (false) and the new (true) vacua. If the barrier at this small temperature is high enough, compared to the thermal energy existing in the system, the field ϕ will remain trapped in the false vacuum state even for small ($< T_c$) temperatures, in other words the domain walls effectively "freeze-out". The typical scale of domain walls at formation is set by correlation length ξ beyond which the fluctuations in ϕ are uncorrelated.
This is a complete picture from classical point of view. However in some regions of space, quantum tunneling effects can free the field from the old vacuum state: there is a probability per unit time and volume in space that at a point $\overrightarrow{x}$ a bubble of true vacuum will nucleate and each of them will has an independent value of the field. This leads again to the formation of domains where the fields are correlated, whereas no correlation exists between fields belonging to different domains. Then after the creation of the bubble, it will expand at the speed of light surrounded by a "sea" of false vacuum domains. As opposed to second-order phase transitions, here the nucleation process is extremely inhomogeneous and $\langle|\phi(\overrightarrow{x})|\rangle$ is not a continuous function of time. To put it briefly, the general feature of the existence of uncorrelated domains became known as the **Kibble mechanism** [5] and it seems to be generic to most types of phase transitions during which "topological defects" arise.

2.3 Cosmic Strings in the Abelian-Higgs model

The symmetry described above is a global symmetry. Its symmetry transformations involve rotating every point in the field by the same constant. A **"local"** symmetry allows each point to vary by a different angle. This symmetry is present in the Abelian- Higgs model described below. The

Lagrangian of the previous example led to an infinite energy density contribution. In the case of the Abelian-Higgs model, a gauge field A_μ will cancel out the divergences, which will lead to an energy density that will no longer be infinite, as happened in the previous section. In this case, the Lagrangian equals:

$$\mathfrak{L} = |D_\mu \phi|^2 - \frac{1}{4} F_{\mu\nu} F^{\mu\nu} - \frac{\lambda}{4}\left(|\phi|^2 - \eta\right)^2 \tag{2.10}$$

where the last term is the same potential as the previous example (2.2), $D_\mu = \partial_\mu - ieA_\mu$ is the covariant derivative and e the gauge coupling. The antisymmetric tensor is $F_{\mu\nu} = \partial_\mu A_\nu - \partial_\nu A_\mu$. This model is invariant under the Abelian group $\mathbf{G} = U(1)$ of local gauge transformations,

$$\phi(x) \to e^{i\alpha(x)} \phi(x), \qquad A_\mu(x) \to A_\mu(x) + e^{-1} \partial_\mu \alpha(x). \tag{2.11}$$

Since the minima of $V(\phi)$ are at $|\phi| = \eta$, this symmetry is spontaneously broken, and the field ϕ acquires a non-zero vacuum expectation value.
To study the properties of the broken-symmetry vacuum, it is convenient to use the gauge in which $\phi(x)$ is real. Then, representing ϕ as $\phi = \eta + \phi_1/\sqrt{2}$, we obtain

$$\mathfrak{L} = \frac{1}{2}(\partial_\mu \phi_1)^2 - \frac{1}{2}\mu^2 \phi_1^2 - \frac{1}{4} F_{\mu\nu} F^{\mu\nu} + \frac{1}{2} M^2 A_\mu A^\mu + \mathfrak{L}_{\text{int}} \tag{2.12}$$

where

$$\mu = \sqrt{\lambda}\eta, \qquad M = \sqrt{2} e \eta, \tag{2.13}$$

and $\mathfrak{L}$ includes higher order than two in ϕ_1 and A_μ. We see that in the breaking of a gauge symmetry does not appear the Goldstone boson. In fact, if the simmetry breaking is local the boson is not present in the spectrum and simultaneously the gauge field becomes massive. The interpretation of this situation is that the boson is “absorbed” as longitudinal mode of the gauge vector. This model was considered by Nielsen and Olesen in their discovery paper on string solutions in relativistic field theories [7].

There is an important difference between global and gauge (or local) cosmic strings: local strings have their energy confined mainly in a thin core, due to the presence of gauge fields A_μ that cancel the gradients of the field outside of it. Also these gauge fields make it possible for the string to have a quantized magnetic flux along the core. On the other hand, if the string was generated from the breakdown of a global symmetry there are no gauge fields, just Goldstone bosons, which, being massless, give rise to long-range forces. No gauge fields can compensate the gradients of ϕ this time and therefore there is an infinite string mass per unit length.

Chapter 3

The variety of defects

Topological defects are at the heart of most SSB based phase transitions. Whenever there is a phase transition based on spontaneous symmetry breaking, topological defects are produced if they are allowed by the structure of the vacuum manifold. These objects should be produced in high-energy particle physics phase transitions just as well as they are produded and, only in this case seen, in low energy condensed matter phase transitions. As has already been mentioned, phase transitions were common in our universe as well when it was young. After its formation, it started to expand and cool down, undergoing several phase transitions related to a series of symmetry breakings. At the beginning, when the universe was very hot, all fundamental interactions were united under the same simple group G (they had the same coupling constant). When the temperature of the universe decreased below some characteristic critic values, T_c , it underwent a series of symmetry breakings related to phase transitions until it reached the present state where all four fundamental forces are decoupled. It is consequently reasonable to expect that during this process, topological defects of cosmological size might have been formed. We can summarize these processes in terms of symmetry groups writing:

$$G \to H \to SU(3) \times SU(2) \times U(1) \to U(3) \times U(1) \tag{3.1}$$

Here, each arrow represents a symmetry breaking phase transition where matter changes form and the groups $-$ $G, H, SU(3), etc.$ $-$ represent the different types of matter, specifically the symmetries that the subject exhibits and they are associated with the different fundamental forces of nature. The basic premise of grand unification is that the known symmetries of the elementary particles resulted from a larger (and so far unknown) symmetry group G. After a phase transition has occurred, the original symmetry G is broken down to H. The group $SU(3)$ is associated with the strong nuclear force, $SU(2)$ is the symmetry group of the weak interaction and the group $U(1)$ is associated with the electric and magnetic forces.

The formation or not of topological defects during the phase transitions, followed by SSB, and the determination of the type of the defects, depends on the topology of the vacuum manifold $\mathcal{M}$. After the phase transition, the order parameter field, that defines the degree of asymmetry in the phase of symmetry breaking, chooses different vacua from this vacuum manifold in different regions of space. These regions form domains in space. During further evolution of the system, the order parameter may get 'locked' in symmetric state in localized regions whenever neighboring domains cover the vacuum manifold in topologically non-trivial [1] manner. Then, there will be some defects. Since these defects are formed due to non-trivial topology of the vacuum manifold, these are called topological defects. The necessary conditions of the formation of such defects depends on various homotopy groups [2] of the vacuum manifold. A theory may have symmetry breaking pattern with vacuum manifold consisting of two or more disconnected pieces. If this occurs, "domain walls" can form, Fig. 3.1.

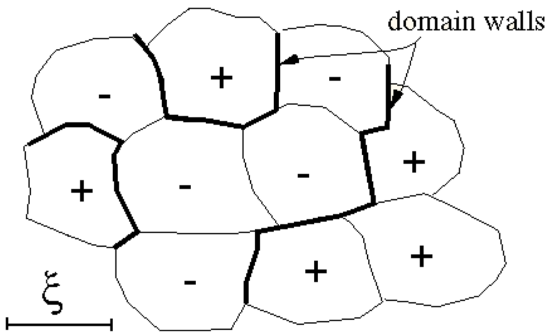

Figure 3.1: Domain walls occur at the boundaries between regions of space.

Similarly, other topological defects, in addition to the domains, like strings, monopoles may arise when the first and the second homotopy group of $\mathcal{M}$ are non-trivial, respectively. Different models for the Higgs field lead to the

[1]The trivial topology on an open set $\mathbf{X}$ is usually defined to be the collection $\{\emptyset, \mathbf{X}\}$. Any other topology on $\mathbf{X}$ is non-trivial.

[2]A homotopy group consists of equivalence classes of maps of spheres (with fixed base point) into the manifold, where two maps are equivalent if they can be smoothly deformed into each other.

formation of a whole variety of topological defects, with very different features and dimensions. In the following, let us provide a review of the most important characteristics of each class of defects. Some of the proposed theories have symmetry breaking patterns leading to the formation of domain walls: two-dimensional thin surfaces appearing at the junction of field values belonging to different disconnected sectors of $\mathcal{M}$, trapping enormous concentrations of mass-energy, similar to two-dimensional sheet-like structures found in ferromagnets. Their appearance is associated with the breaking of a discrete symmetry. Domain walls occur at the boundaries between regions of space with values of the field ϕ in different components, with ϕ interpolating between these two values across the wall. The model generally considers a set of real scalar fields ϕ_i with a Lagrangian of the form

$$\mathfrak{L} = \frac{1}{2}\left(\partial_\mu \phi_i\right)^2 - V\left(\phi\right) \tag{3.2}$$

where the potential $V\left(\phi\right)$ has a discrete set of degenerate minima.
Within other theories, cosmological fields are distributed in such a way that the old symmetric phase is confined into a finite region of space surrounded by the new and non-symmetric phase. This situation evolves into the generation of defects with linear geometry called "cosmic strings", Fig. 3.2.

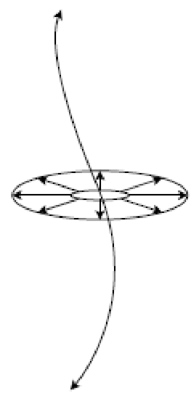

Figure 3.2: Cosmic string appears as a line.

The strings arise in models in which the vacuum manifold $\mathcal{M}$ is not simply connected, so it contains enclosed holes about which loops can be trapped. Theoretical reasons suggest these strings (vortex lines) do not have any loose ends in order that the two phases not mixed up. This leaves infinite strings and closed loops as the only possible alternatives for these defects to manifest

themselves in the early universe. In other words, it can be stated that cosmic strings are infinitely long and filamentary remnants of primordial dark energy which formed in the early universe and were then stretched by the expansion of the universe up to the point that, at present epoch, some cosmic strings could cross the entire length of our observable universe.
By analogy with strings, point like defects or monopoles, Fig. 3.3, arise if the manifold of degenerate vacua contains non-contractible two-surfaces (like the sphere S^2).

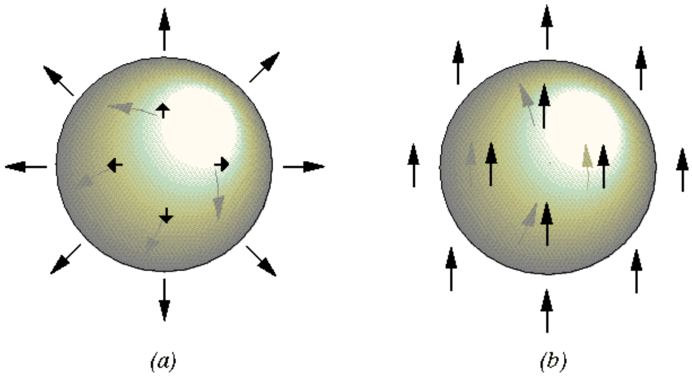

Figure 3.3: A field configuration on a two-sphere signalling the presence of a monopole within. In particular, the three-dimensional "hedgehog" configuration corresponds to a monopole.

With a bit more abstraction, scientists have even conceived other (semi) topological defects, called "textures", in Fig. 3.4.

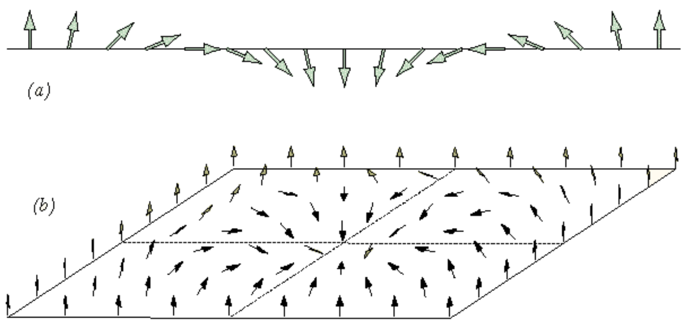

Figure 3.4: Examples of texture configurations in one (a) and two (b) dimensions, corrisponding to the winding of a field about circular vacuum manifold.

These are conceptually simple objects, yet, it is not so easy to imagine them for they are just global field configurations living on a three-sphere vacuum manifold (the minima of the effective potential energy), whose non-linear evolution perturbs space-time. In contrast to domain walls and cosmic strings, textures have no core and thus the energy is more evenly distributed over space. Secondly, they are unstable to collapse and it is precisely this last feature that makes these objects cosmologically relevant. In so doing, it should be evident already that the topology of the vacuum manifold $\mathcal{M}$ determines whether defects appear at a particular symmetry breaking.

The relevant properties of the manifold $\mathcal{M}$ are studied using homotopy theory, so in order to classify qualitatively defects we can use the n^{th} homotopy group $\pi_n(\mathcal{M})$. More generally, the topological defects of a particular dimensionality arising in a given model can be classified by the elements of the appropriate homotopy group of the vacuum manifold $\mathcal{M}$. Table 3.1 summarizes the correspondence between defects and the homotopy group.

Topological defect	*Dimension*	*Classification*
Domain walls	2	$\pi_0(\mathcal{M})$
Strings	1	$\pi_1(\mathcal{M})$
Monopoles	0	$\pi_2(\mathcal{M})$
Textures	–	$\pi_3(\mathcal{M})$

Table 3.1: Topological classification of defects with the homotopy groups $\pi_n(\mathcal{M})$.

In this framework, we focus on cosmic strings. Cosmic strings are without any doubt the topological defect most thoroughly studied, in both cosmology and solid-state physics. In fact, they exist in many field theories motivated by particle physics, and this suggests that they may exist on a larger scale in the universe, hence the name **"cosmic" strings**. In cosmological applications, strings are generally curved, dynamical, and may form closed loops. The energy of a string is concentrated along an infinite line and remains concentrated there for a duration that is very long compared to the dynamical time of the string.

Depending on the energy scale of symmetry breaking, local monopoles and domain walls can have catastrophic cosmological effects, since they might dominate the energy density of the universe. Local textures are not cosmologically significant, as they decay quickly with time. Strings, on the other hand, are far more interesting because they find their natural explanation in the inflationary scenario and are fully predicted by a wide class of elementary particle models, and they will be studied extensively throughout this thesis.

3.1 Other cosmic string models

In addition to elementary defects previously mentioned, the cosmic zoo includes other species of "animals". The physical properties of these defects can be very different depending on whether they are formed as a result of gauge or global symmetry breaking. Here, we give a brief description of some possible configurations of defects. The list below is not complete and furthermore there are some defects that fit more than one category. For more details, we refer the discussion to the reviews by Vilenkin and Shellard [6], Hindmarsh and Kibble [8].

- **Wiggly strings**
  The name wiggly strings is sometimes used to denote any type of string whose mass per unit length is different from its tension μ (the main parameter to describe a string, see Chapter 4). In the simple relativistic strings, the mass per unit length and the string tension are equal, because of Lorentz invariance under boosts along the direction of the string, but this need not be true for more elaborate models. The wiggles, some small structures, on the string produce a renormalized effective mass per unit length $U > \mu$ and an effective tension $T < \mu$. Moreover, the presence of currents along the strings seems to influence the mass and the tension. A particular kind of these small structures is found in extra dimensional models. In fact, if there are more than the three spatial dimensions we observe, strings may be able to wrap around the extra dimensions leading to a renormalized four-dimensional tension and mass per unit length.
  The presence of extra dimensions provides a further energy flux mechanism (as energy may be lost into or gained from the extra dimensions), which will affect the string dynamics.

- **Non-topological, embedded, electroweak and semilocal strings**
  In the Nielsen-Olesen model, the scalar field is zero at the core of the string, and the symmetry is unbroken there. The zero field is protected by the topological properties of the vacuum manifold and the string is called **topological**. These strings are unbreakable and stable. There are cases in which there is no topological protection but the strings are nevertheless stable. The scalar field configuration at the core can be deformed continuosly into a ground state, so these **non-topological** strings can break. Whether this happens depends on the masses and couplings of the particles present, on the temperature, etc. Examples of these types of strings are the "embedded" and the "electroweak" strings, that carry magnetic flux of the Z boson. They are closely

related to "semilocal" strings, another example of embedded strings where the symmetry breaking involves both local and global symmetries interwined in a particolar way. Semilocal strings play a fundamental role: their very low mass makes them remarkably stable. So they can form networks as a collection of segments which then grow and reconnect to form longer strings or loops. Furthermore, using Planck mission dataset [2], the study reported in the paper by Sazhina & Scognamiglio [9] claims the semilocal strings as the most preferred one.

- **Dressed and Superconducting strings**
  If a stable string traps in its core any particles whose mass is lower inside due to interactions with the scalar field, the string is called "dressed". In extreme cases, the mass of these trapped particles is zero in the core and they lead to persistent currents along the strings, which are then known as "superconducting".

- **Hybrid network**
  Hybrid network is made by more than one type of defect, such as for instance strings of different kind or composite defects combining strings, monopoles and/or domain walls. It can happen that the hydride network contains different types of strings linked by junctions and bridges. Interesting is also the case in which two types of strings each carrying different type of flux that is separately conserved. Their name is "(p,q) strings", where p and q are numbers that refer to the units of each kind of flux carried by the strings. Finally, the case in which a string has monopoles at its ends: the union of such elements are called "necklace". We wanted to provide a very brief outline of the other types of defects and refer the reader to the paper by Achùcarro & Martins [3] for more details.

3.2 The Cosmic Superstrings

The recent interplay between superstring theory and cosmology has led to the notion of cosmic superstrings [12], providing the missing link between superstrings and their classical analogues. The ideas of cosmic strings and superstrings emerged at about the same time, but were initially unrelated. In 1985, Witten was the first to consider the possibility that fundamental strings produced in the early universe could progressively stretch to cosmic size. Unfortunately, this possibility was quickly ruled out for several reasons. First the string energy scale is close to the Planck energy (about $10^{19} GeV$), and so the superstring tension μ would be too high: $G\mu \gtrsim 10^{-3}$, while it was

clear even then that for cosmic strings $G\mu \lesssim 10^{-5}$, otherwise they would generate excessively large perturbations. Secondly, any period of inflation would have diluted the numbers of pre-existing cosmic strings or superstrings to an unobservable level; only strings formed after or at the end of inflation could be observationally relevant.
According the **String Theory**, the fundamental constituents of matter are not point particles but one-dimensional strings, either open or closed (forming loops), whose vibrational modes produce all elementary particles and their interactions. Two important features of the theory are supersymmetry and the presence of extra dimensions, namely the brane-world scenario (a multi-dimensional space-time when additional spatial dimensions have certain properties) [11]. In fact, the theory can only be made consistent in a space-time of more than the conventional four dimensions that we observe - 26 for bosonic strings or 10 for superstrings - , which incorporate supersymmetry, connecting bosons and fermions. But why can we only perceive four dimensions? Where are the other six dimensions? The theory tells us that the additional dimensions can be perceived and "seen" only on an infinitesimal distance, as they are folded on themselves and therefore beyond our direct knowledge (and perhaps even indirect). One way of reducing the number of dimensions is the Kaluza-Klein mechanism, in which it is assumed that the remaining six dimensions are compactified, resulting in an effective 4-dimensional space-time we live in. The superstrings have been considered as possible cosmological objects in accordance with the fact that their energy can be significantly lower than the Planck one. Thus, the tension of the cosmological superstrings would be comparable with the observational limits. This approach is implemented in the representation of brane-world. In the 4D space-time fundamental superstrings can not be stretched to the cosmological scale, they "tear" and will become a system of microscopic superstrings. In the brane-world scenario, an extra dimension reduction provides the existance of superstrings on the cosmological scales.

More generally, **M-theory**, contains the brane-world scenario, in which the fundamental objects are two-dimensional "membranes" and the background space-time is 11-dimensional. The M-theory combines the five theories of the strings, showing that they are, essentially, different descriptions of various aspects of the same theory. The five theory, that can be distinguished by the form of strings and how they implement the supersymmetry concept, are listed here:

- Type I
- Type IIA

- Type IIB
- Type $SO(32)$
- Type $E_8 \times E_8$

The common property of these models is that ordinary matter is concentrated on the hypersurface, the brane, immersed in a space-time of higher dimension, called the bulk and the gravity can be spread in it (for review, see [10]). From this perspective, our universe may be one of such a brane. Finally, the superstring can naturally appear in brane-world scenario with energies that are comparable with observational constraints on cosmic string energies.

Chapter 4

Searching for Cosmic Strings in astrophysical data

Despite the complexity of the cosmological scenario, that still stands in the way of a complete understanding of cosmic strings, a promising strategy is described here, aimed at detecting these elusive physical entities. The procedure presented in this work is a combination of two modern methods for CS observational search: the analysis of the anisotropy of the Cosmic Microwave Background (CMB) radiation, looking for step-like discontinuities in gradient of CMB temperature and the strong gravitational lensing effects on background sources by a CS.
We must stress that the optical and CMB methods provide complementary informations and in order to provide definitive results they must be used in conjunction.

4.1 First method: cosmic strings signature on CMB maps

In 1964, Bell Labs scientists Arno Penzias and Robert A. Wilson were conducting experiments with the Holmdel Horn Antenna, an extremely sensitive device originally used to detect radio emission from the Cassiopeia A supernova remnant, when they detected a uniform noise source, which was assumed to come from the apparatus. Despite taking all conceivable steps to eliminate interference, checking the antenna and the electronics (including removal of a birds nest from the horn), they continually detected a strange, buzzing noise that was coming from all parts of the sky at all times of day and night. They ultimately concluded that the signal, corresponding to a black body radiation with a temperature of $2.7K$ [1], might actually be coming from outside of our galaxy. Almost by chance, they later learned that researchers and astrophysicists Robert H. Dicke, Jim Peebles and David Wilkinson at nearby Princeton University were looking for a way to detect residual radiation that they believed would have resulted from the Big Bang. As it turned out, the radiation detected by Penzias and Wilson was a perfect match for what the Princeton researchers had predicted, and it was a success of the Big Bang model.

Since then, there have been many advances in observational cosmology and quantitative cosmological constraints now came from a number of complementary investigations. What we observe today in the radio maps is the variation in temperature of the CMB: nothing more than a snapshot of the local properties (density, peculiar velocity and the total gravitational potential) of the gas of CMB photons at the time the primordial plasma recombined at redshift $z \approx 1100$.

As it was outlined in the previous chapter, in its early history the universe has gone through phases where it was in different regimes of the energy density: matter, radiation, and dark energy. The matter consisted of all known elementary particles and included a dominant component of dark matter, stable and massive particles with negligible electromagnetic interactions. Initially, matter and radiation were in thermal equilibrium. As the universe expanded, particle energies (and hence the temperature of the universe) decreased. The universe was initially radiation dominated and most of its energy density was in photons, neutrinos, and in their kinetic motion. After the universe cooled to the point at which the energy in rest mass equaled that in kinetic motion (matter - radiation equality), the expansion rate slowed and the universe became matter dominated, with most of its energy connected to the slow motion of relatively heavy stable particles: among the baryons, mainly protons and deuterons, plus the already mentioned dark matter particles. When the universe became sufficiently cool, electrons and protons combined to form hydrogen atoms. Before this happened, the photons could not travel far, as they were continuously absorbed and re-emitted by the charged particles in the universe. After recombination, the universe was neutral, photons come to us from this surface of last scattering with no further interactions, save the red-shifting due to the expansion, because they are able to travel long

[1] There is a finite time interval during which decoupling took place and during it approximately all interactions between photons and matter were elastic scattering processes (i. e. Thomson scattering). In those processes the frequency of a photon does not change, therefore the conclusion that the spectrum of the photons remains a black body spectrum still holds.

distances (the universe become "trasparent"). The radiation we see today in the CMB was produced at this very remote epoch.
From the very beginning, cosmologists began searching for anisotropies in the background radiation and, despite of the numerous experiments, aimed to detect the large-angle temperature anisotropies, they were first discovered by RELIKT-1 in 1992 [14]. After it, several instruments (COBE-DMR, RELIKT-2, etc) have mapped the anisotropies and we now have high quality measurements of the statistics of the anisotropies: we will focus on the WMAP satellite and on a third-generation CMB satellite, Planck.

The anisotropy of the CMB consists of the small temperature fluctuations in the blackbody radiation, superimposed on the average of $2.7K$. The anisotropies of the CMB are classified in primary and secondary:

- The **primary anisotropies** are the CMB fluctuations generated before recombination;

- The **secondary anisotropies** are the CMB fluctuations generated following recombination.

All temperature fluctuations in the microwave background are due to one or more among the following effects:

- A change in the intrinsic temperature of radiation at a given point in space. This will occur if the radiation density increases via adiabatic compression, just as with the behavior of an ideal gas. The fractional temperature perturbation in the radiation just equals the fractional density perturbation;

- A Doppler shift if the radiation at a particular point is moving with respect to the observer. Any density perturbations within the horizon scale will necessarily be accompanied by velocity perturbations. The induced temperature perturbation in the radiation equals the peculiar velocity, with motion towards the observer corresponding to a positive temperature perturbation;

- A difference in gravitational potential between a particular point in space and the observer will result in a temperature shift of the radiation propagating between the point and the observer due to gravitational redshifting. This is known as the Sachs-Wolfe effect.

The result of temperature fluctuations is the basic observable of the CMB: the power spectrum, that is the CMB intensity as a function of frequency and direction on the sky $\hat{\mathbf{n}}$ (being radiation anisotropic). Since the CMB spectrum is an extremely good blackbody [32] with a nearly constant temperature across the sky, T, we generally describe this observable in terms of a temperature fluctuation

$$\Omega(\hat{\mathbf{n}}) = \Delta T/T. \tag{4.1}$$

In the hypothesis of Gaussian fluctuations, we consider the multipole decomposition of the temperature field in terms of spherical harmonics Y^*_{lm}

$$\Omega_{lm} = \int \Omega\left(\hat{\mathbf{n}}\right) Y^*_{lm}\left(\hat{\mathbf{n}}\right) d\hat{\mathbf{n}} \tag{4.2}$$

The field is fully characterized by its power spectrum $\Omega^*_{lm}\Omega_{l'm'}$, where the order m describes the angular orientation of a fluctuation mode, and the degree (or multipole) l describes its characteristic angular size. Thus, in a universe with no preferred direction, we expect the power spectrum to be independent of m. Finally, we define the angular power spectrum C_l by

$$\langle \Omega^*_{lm}\Omega_{l'm'}\rangle = \delta_{ll'}\delta_{mm'}C_l \tag{4.3}$$

where the brackets denote an ensemble average over skies with the same cosmology, so the set of C_l forms the power spectrum that shows the intensity of the harmonics at variation the multipole order. Fig. 4.1 shows the trend of the power spectrum: it is relatively flat for $l < 20$, the main peak is present for $l \sim 200$ and represents the most important feature of the power spectrum.

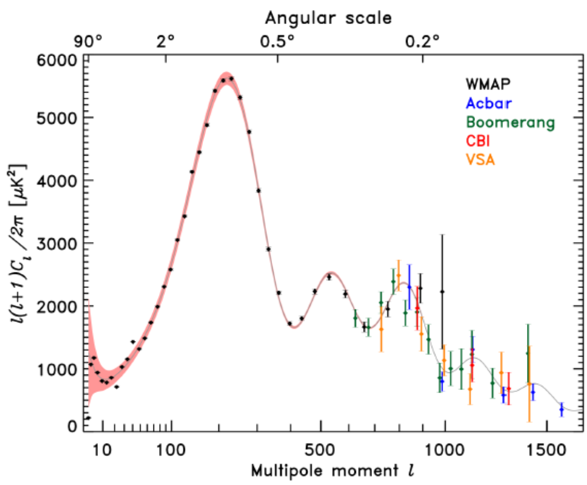

Figure 4.1: CMB power spectrum with data from WMAP, and high-l data from other experiments.

Such a peak, called "acoustic peak" and indicates that at a particular angular scale the anisotropies are maximum. The acoustic peak is followed by a series of lower oscillations, while spectrum declines rapidly for $l > 1000$. In addition to temperature fluctuations, the decoupling, since the Thomson scattering which couples the radiation and the electrons is not isotropic but varies with the scattering angle, inevitably leads to non-zero polarization of the microwave background radiation. Some of the CMB radiation is linearly polarized, thanks to the fact that most electrons at the surface of last scattering see a quadrupole temperature anisotropy around them, however quite generically the polarization fluctuations are expected to be significantly smaller than the temperature fluctuations.

In this way, the CMB anisotropies encode information on the primordial perturbation itself, as well as on the matter composition and geometry of the universe. This also implies that any topological defects resulting from the formation of the universe must have left its signature, in fact, they are expected to induce discontinuities in the anisotropy of the CMB [6], [31], [35]. This method offers two advantages: the background source (CMB) is the most distant source in the universe (redshift ~ 1000) or, equivalently, it is the closest source to the particle horizon of our universe. Therefore, all the cosmic strings which are inside the observable part of the universe will affect the CMB. The second advantage is that multi-frequency all-sky surveys of the CMB already exist and despite of the low sensitivity, the studies have allowed to set upper limits [38].

4.1.1 Search for anisotropy of CMB induced by a solitary CS by modified Haar wavelets in Planck and WMAP radio data

The peculiar topology of the space-time in presence of a string can cause a detectable effect in the cosmic microwave background, by giving a contribution to its anisotropies. In fact, if we consider a solitary, long and straight CS moving with a constant velocity v, owning to the tension (linear density) μ against a homogeneous and isotropic background [36], its moving may generate anisotropy in the CMB due to the simple Doppler mechanism. This is known as the Kaiser–Stebbins effect [39]: a moving CS induces a relative speed between the light source and observer and causes a shift of photons.
Consider two particles moving towards the string along parallel paths with the same velocity v. As they pass the string, the particles start moving towards one another and eventually collide. The relative velocity of the par-

ticles after they pass the string is

$$\delta u = \beta\gamma\Delta\Theta \tag{4.4}$$

where $\Delta\Theta = 8\pi G\mu$ ($c = 1$) is the deficit angle, which is the angle of the 3D space of the cone, which replaces the 3D Euclidean space of our universe in the presence of a cosmic string [6] and β ($c = 1$) is the projection of string velocity on the line perpendicular to the one joining the source and the observer, in unit of c. The Lorentz factor, $\gamma = (1-\beta^2)^{-1/2}$, appears after transforming to the reference frame of one of the particles, and assuming that the line connecting the particles is perpendicular to the string direction. If one of the objects is a source of radiation and the other is an observer, then the observer will detect a discontinuous change in the frequency of radiation due to the Doppler shift. In a cosmological setting, the string is backlighted by a uniform black-body radiation background, and the Doppler shift results in a discontinuous change of the background temperature across the string [39]. The magnitude of this variation is:

$$\frac{\delta T}{T} = \delta u = 8\pi G\mu \frac{\beta}{\sqrt{1-\beta^2}} = 8\pi G\mu\beta\gamma \tag{4.5}$$

According to this model [36], an anisotropy induced by solitary CS represents a sequence of zones of decreased and increased temperature: the cold spot in front of moving string, the step-like jump, and then appearance of hot spot; finally a cold spot follows again . The total effect is a step-like discontinuity in the CMB temperature distribution as depicted in Fig. 4.2.

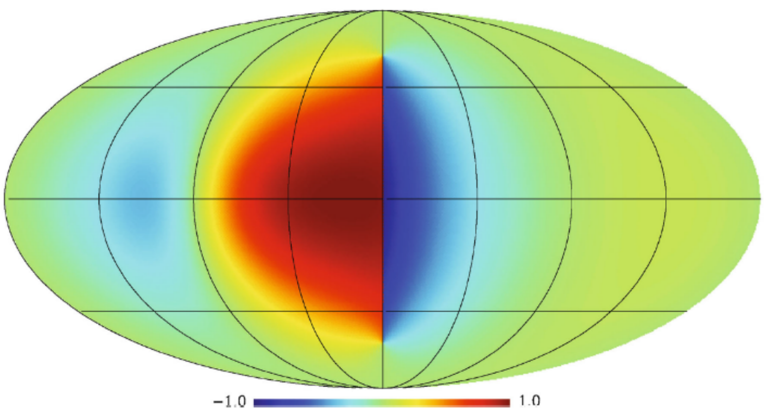

Figure 4.2: The Mollweide projection of the sky shows simulated structure of anisotropy (temperature variation) induced by one straight CS lying on the line connecting the north and south Galactic pole. A string is moving relativistically from the left to the right.

It is possible to generalize equation (4.5) for arbitrary angles between the string, its velocity, and the line of sight [13], [15].

Due to the specific discontinuity structure of CS anisotropy and its low amplitude we searched its traces with a special step-like set of orthogonal functions, convolving the ordinary maps (obtained in the radio) with a modified Haar functions (MHF), Fig. 4.3.

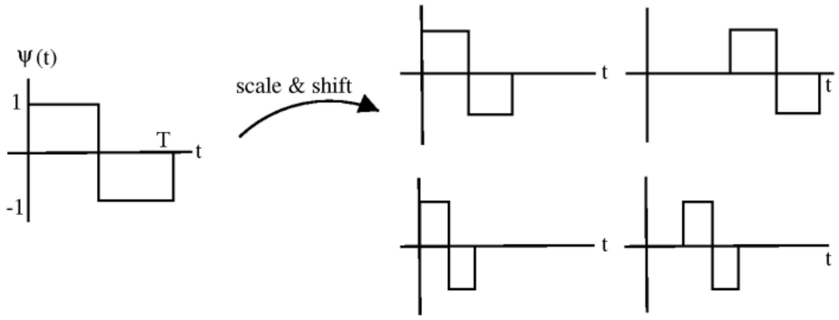

Figure 4.3: The basic Haar function and the scaled and translated versions of a "mother wavelet" $\Psi(t)$.

The convolution procedure is the standard technique based on the use of the most appropriate and complete orthonormal system. In our case of a step-like signal the choice is the MHF set. The modified Haar harmonic is most sensitive to the appearance of discontinuities in radio survey data, in fact this technique is able to detect a CS at a level of $\delta T \approx 10\mu K$ [37]. Let we show how to get it in the following. In principle, we could expand our data in ordinary trigonometric functions of the angular coordinate of the disk (e.g. $sin\varphi$ and $cos\varphi$) and in some set of functions that are orthogonal to the disk radius. However, generally speaking, expansion in functions (of an angular variable) of any other form implies that the signal power is distributed over all the harmonics. Thus, when expanded in trigonometric functions of the angular anisotropy due to the CS, the amplitudes of all the harmonics will be non-zero. In other words, the signal from the CS will be smeared out over the entire spectrum. In order for the signal to be detected, the power smeared out over all the harmonics must be "gathered" to make use of the full power of the signal. For our purpose the MHF is a realization of the first harmonic of the Haar system of orthogonal functions with cyclic shift. This function is equal to 1 in the rotation range $[0, \pi)$, and it is equal to -1 in the rotation range $[\pi, 2\pi)$. The rotations result in a set of amplitudes. Since a CS could be oriented arbitrarily with respect to a grid of lines of longitude and latitude, the search for a CS at each point requires multiple convolutions with a rotation of the circle, which corresponds to a shift in the "jump" in the Haar function. This shift yields a new orthogonal and complete set of functions: MHF. When there is a CS at a convolution point, the harmonic is maximum if a chord of the circle coincides with the position of the CS. We assigned each pixel a value equal to the corresponding maximum value of the convolution, making a map of CS candidates as in Fig. 4.4.

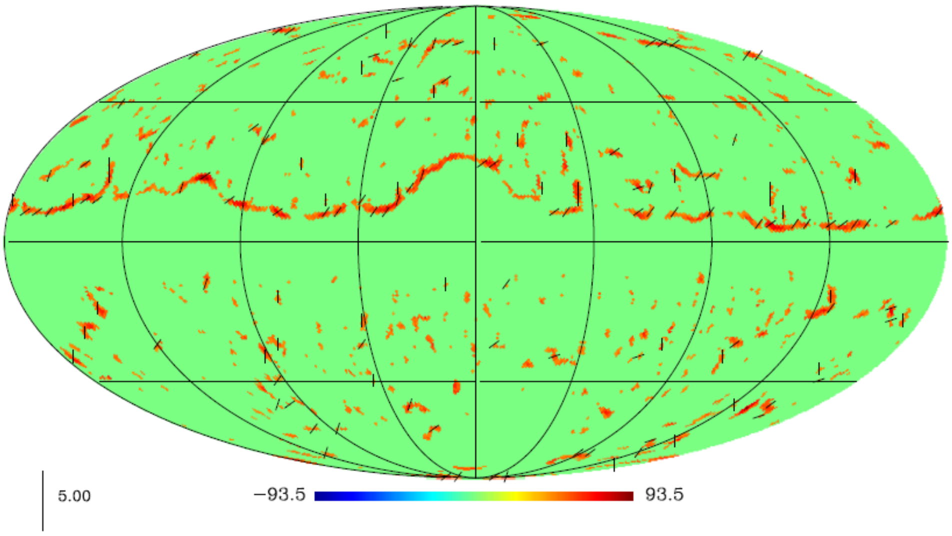

Figure 4.4: CS candidates (continuous zone with indication of temperature gradients) in Planck data after MHF analysis at the 3σ level. Units are $[\mu K]$. The radius of the MHF convolution is $5°$. The long continuous traces in the vicinity of the Galactic equator are the remnants of the Galactic filter.

Before the MHF algorithm was applied on real data, the WMAP and Planck data, we estimated its efficiency and chose the optimal convolution circle radius [16]. The MHF algorithm was applied to process a map that is a sum of two model maps: the first map is a simulated map of the primordial CMB anisotropy that arose at the surface of last scattering and the second one is a pure anisotropy generated by a straight, moving CS (see Fig. 4.2 as an example of such map). The maps of the primordial CMB anisotropy and the anisotropy generated by the moving CS were summed with a coefficient to characterize the signal-to-noise ratio. To choose an optimal circle radius for a search for CS, computer simulations were executed to obtain maps of the distribution of the harmonic amplitude for circles with various radii. So, the CS detection was characterized by the signal-to-noise ratio, since the CS position in the model maps was known. The amplitude at the CS location was taken to be the signal and the rms of the harmonic amplitude in the map to be the noise. Those simulations indicate that the optimal value of the convolution circle radius is from 3° to 5°. In order to study the efficiency of the MHF algorithm, statistical methods of simulations were also apply, creating a robust set of 300 maps of sky simulating the CMB structure without any string. The results show that there are less than one false string candidates in simulations: this is considered a strong support to the efficiency of the process [16]. The Figg. 4.5 and 4.6 show examples of simulated maps and the result of them after the application of MHF algorithm.

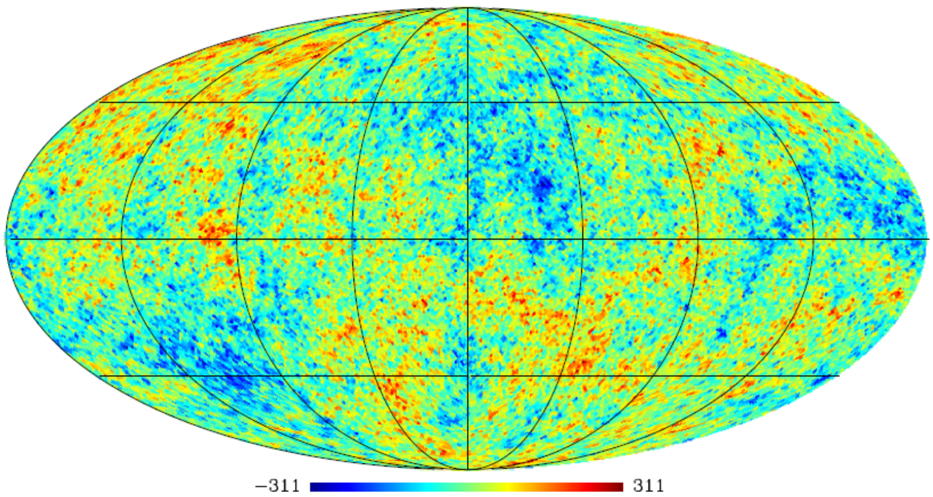

Figure 4.5: Simulated CMB map. Units are [μk].

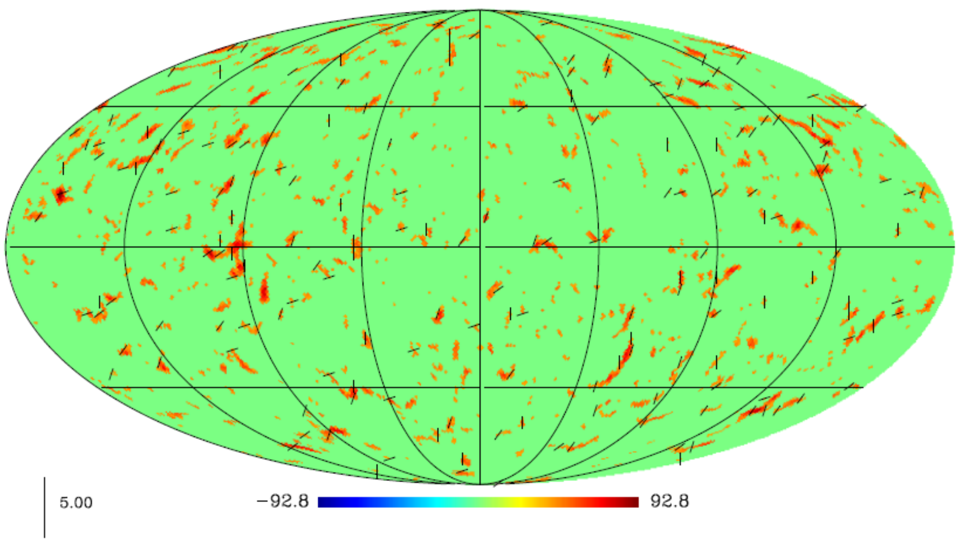

Figure 4.6: False CS candidates for simulated CMB map Fig. 4.5. Units are [μk].

In order to find CS candidates (see Fig. 4.4), we prepared six independent original Planck maps (from 100 to 857 GHz) cleaning them with recommended Galaxy filters and point source extractors [2]. The cleaned maps are convolved in each pixel with a MHF specified in a circle, see Fig. 4.7 as a cleaned map example for 143 GHz.

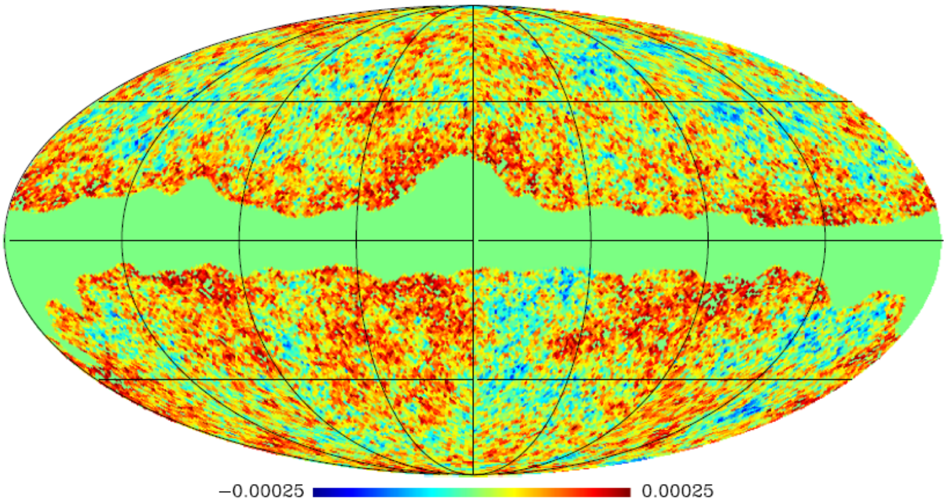

Figure 4.7: Cleaned Planck data map for 143 GHz, with 70% Galaxy mask. Units are $[K]$.

We use two main necessary conditions to handle found structure as CS candidate:

- a continuous line, that represents the best match between the Haar step-like function and the "jump" on CMB map;
- at least three correlated vector of temperature gradients.

We applied this procedure to all the available wave-channels 100, 143, 217, 353, 545, 857 GHz for different sky coverage of 70, 80, 90, 95, 97, 99 %. The sky coverage characterizes the type of Galactic mask [2]. Of course, in this process we reject some candidates lying in the equatorial Galactic region since that region gives spurious contributions to the radiation emission. Furthermore, all available filters were used to compare the positions of the candidates and filter out those which are not present at all frequencies, as the appearance of a real CS shall not depend on the observation frequency. The result of CS candidates search by MHF algorithm applied to Planck data is shown for filter 143 GHz, in the following Table 4.1.

CS candidate number	*CS tension*	*Sky coverage*
3	5.52	97
2	5.66	99
2	6.15	90
2	6.32	70
1	7.07	99
1	7.36	97

Table 4.1: The result of CS candidates search by MHF algorithm applied to Planck CMB data for filter 143 GHz. CS tension in unit of (10^7).

These results comes from the relation between the tension μ and the number of the cosmic strings. For example, for the filter 143 GHz, the 1σ value corresponds to $\delta T = 14.8\ \mu K$ but in this case we have some wrong candidates which have to be studied by additional optical methods (search for an excess of gravitational lensing events nearby the CS candidates). The 2σ and 3σ levels correspond to 29.6 μK ($G\mu/c^2 = 4.21 \times 10^{-7}$) [10] and 44.4 μK ($G\mu/c^2 = 6.32 \times 10^{-7}$), respectively. We found that there are no CS with tension more than $G\mu/c^2 = 7.36 \times 10^{-7}$. For tensions in the range $G\mu/c^2 = 6.44 \times 10^{-7}$ to $G\mu/c^2 = 7.36 \times 10^{-7}$ we have no more than one CS candidate. For the lowest tension limit available by the MHF algorithm, we have no more than five CS candidates in the whole universe inside the last scattering surface. For $G\mu/c^2 \leq 4.83 \times 10^{-7}$ the MHF method is ineffective because of unverifiable or even wrong CS candidates. Thus, the existence of string with tensions $G\mu/c^2 \leq 4.83 \times 10^{-7}$ is not excluded, but it is beyond the Planck data possibilities.

Finally, our MHF algorithm with the results in [2] made it possible to clarify the preferred CS types. The most preferable types of CS are semilocal ones, described by the model with complex scalar doublet [6]. If its imaginary part is equal to 0, the semilocal CS becomes the Abelian-Higgs CS. The main difference between these two types of CS is that the semilocal CS can have ends (monopoles) and can be unstable under certain conditions. The topological ("ordinary") CS have no end and formally, they break on the surface of last scattering. It means that if our CS candidates are topological defects, then they have to be very far from the observer, up to $z = 7$, because their length is much less than $100°$ [36]. In this case we have no possibility to observe their effects in the optical data by looking through gravitational lensing events, and we will never confirm our candidates by independent optical observation. But the situation substantially changes if we are dealing with semilocal CS. They can be closer to us, being not very long. Therefore, our strategy is now to find suitable optical fields to search for the chains of gravitational lenses, produced by candidates semilocal CS. The structure of the CS candidates found by the MHF method confirms the view of semilocal CS as a collection of segments (for the detailed study we remand to [9]).

Following the above criteria, we select the best map, with $\delta T/T = 38.5\mu K$, hereinafter referred to as **CSc-1**. The identification of it was done in IDL system with the HEALPix package, which is designed to generate and analyze sky maps. It has been used the IDL-program (developed by M.V. Sazhin and O.S. Sazhina) for cosmic string search with the MHF method. Using as input the ILC-Plack map [2] it was identified the string candidate CSc-1 with the higher level of the standard deviation (s.d.), calculated over all sky map after the Haar convolution. Using the HEALPix operators 'mollview' and 'mollcursor', we define the galactic coordinates of the containing region the CSc-1, Fig. 4.8, which will be the issue being addressed in the later optical analysis.

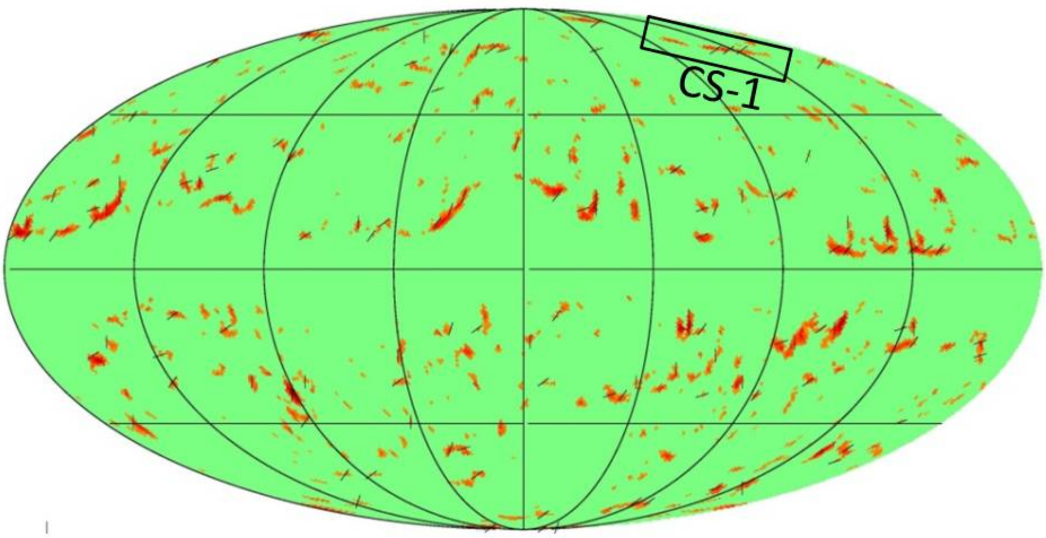

Figure 4.8: The Mollweide projection of the CMB anisotropy map after the MHF-convolution and the cosmic string candidate CSc-1 is indicates with the rectangular frame. The amplitude of the CSc-1 is $\approx 40\mu K$ under the original CMB background of the order of $100\mu K$. There are indicated the temperature gradients which have to be correlated.

[2]The ILC is a technique of the NILC method applied to multi-channel observations in needlet space, with weights that are allowed to vary over the sky and over the full multipole range, in order to extract the CMB (or any component with known spectral behaviour).

4.1.2 The CMB explorers

- **WMAP**
  The Wilkinson Microwave Anisotropy Probe also known as WMAP, and Explorer 80 is a spacecraft which measures differences in the temperature of the CMB across the full sky, Fig. 4.9.

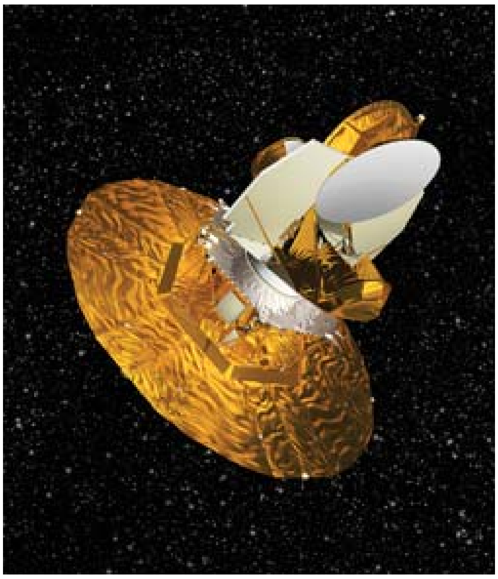

Figure 4.9: WMAP spacecraft.

WMAP is named in tribute to American physicist David Todd Wilkinson, who died in 2002 and he had been a member of the mission's science team. The WMAP spacecraft was launched on 30 June 2001 from Florida and was positioned near the second Lagrangian point (L2), a gravitational balance point between Earth and the Sun and 1.5 million km opposite the Sun from Earth.
Data from WMAP showed temperature variations of $0.0002K$ caused by intense sound waves echoing through the dense early universe, about 380,000 years after the Big Bang. This anisotropy hinted at density variations where matter would later coalesce into the stars and galaxies that form today's universe. WMAP determined the age of the universe to be 13.8 billion years, measured the composition of the early, dense universe, showing that it started at 63% dark matter, 12% atoms, 15% photons, and 10% neutrinos. The contribution of dark energy at the time was negligible. It also used to universe's geometry and to the Big Bang model and the cosmic inflation theory. For that, the mission created a full-sky map of the CMB, with a 13 arcminute resolution via

multi-frequency observation. The map requires the fewest systematic errors, no correlated pixel noise, and accurate calibration, to ensure angular-scale accuracy greater than its resolution. The map contains 3,145,728 pixels, and uses the HEALPix scheme to pixelize the sphere. The telescope also measured the CMB's E-mode polarization and foreground polarization. WMAP was initially planned to operate for two years, but its mission was extended to September 2010 and in 8 years, three different data releases were produced.

- **Planck**
  Planck is the latest space observatory operated by the European Space Agency (ESA) from 2009 to 2013 and it mapped the anisotropies of the CMB at microwave and infrared frequencies, with high sensitivity and small angular resolution, Fig. 4.10.

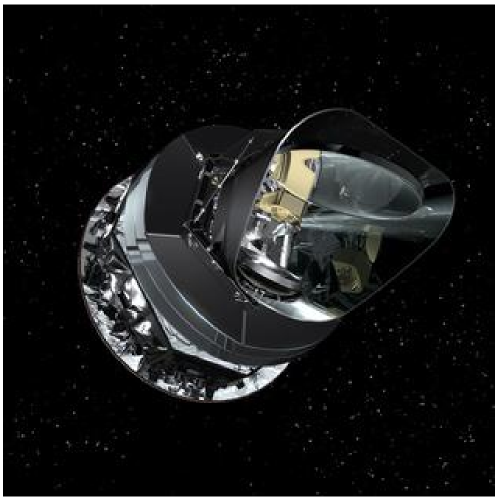

Figure 4.10: The Planck satellite.

The project, initially called COBRAS/SAMBA, was later renamed after its approvals, in honour of the German physicist Max Planck. Its features are listed below:

- The spacecraft carries two instruments: the Low Frequency Instrument (LFI) and the High Frequency Instrument (HFI), both can detect the total intensity and polarization of photons;
- Covered frequency range: 30 to 857 GHz;
- Sensitivity: $\Delta T/T \sim 10^{-6}$;
- Angular resolution: 5 arcmin.

4.2 Second method: strong gravitational lensing by a CS

Gravitational lensing is a consequence to General Relativity: when photons from distant sources travel across the universe, their trajectories are perturbed by the distribution of matter. In particular, their paths are deflected by an angle due to the local curvature of space-time; in the "strong lensing" regime this can produce multiple images, in the simplest case double images. Let us discuss the theoretical features of a CS as gravitational lens.

The gravitational properties of cosmic strings are deeply different from those of non-relativistic matter. This can be easily seen in the toy model case of a static and straight cosmic string, where in the weak field limit, the Einstein field equations are

$$\nabla^2\phi = 4\pi G\left(\rho + 3p\right) = 0 \tag{4.6}$$

where ϕ is the gravitational field, ρ the energy density and p is the pressure. For a cosmic strings $p = -\rho/3$, in the hyphotesis of a universe dominated by radiation. A cosmic string affects the global geometry of space-time around it: Vilenkin (1981) first studied the gravitational properties of cosmic strings under the weak field approximation. He found that the metric describing the space-time around a straight cosmic string in cylindrical coordinates (assuming that the cosmic string lies on the z-axis) has the form

$$ds^2 = dt^2 - dz^2 - dr^2 - r^2 d\theta, \qquad 0 \leq \theta < 2\pi\left(1 - 4G\mu\right). \tag{4.7}$$

This is the Minkowskian metric of the space-time, but with the angular coordinate not allowed to vary up to 2π. The effects of such a geometry can be seen in the trajectories of two test particles moving in parallel towards a cosmic string, which is perpendicular to their motion plane as shown in Fig. 4.11.

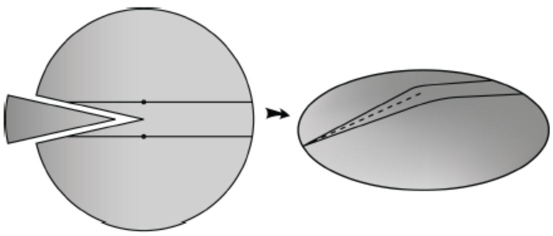

Figure 4.11: In the space-time around a cosmic string, the trajectories of two test particles as they move perpendicular to it. The cosmic string's axis passing through the top of the cone.

Photons from a background source move around the CS, and by circumnavigating the CS, they form two images on its sides. Since along the two trajectories the space is flat, there is no gravitational attraction exerted by the CS on the photons and no distortion is introduced. However, in spite of the fact that the metric is locally flat, the global properties of the space-time are not Minkowskian but conical, and a complete revolution around the position of the CS, gives a total angle that is smaller than 2π; the difference is called "deficit angle", Fig. 4.12:

$$\Delta\Theta = 8\pi G\mu, \tag{4.8}$$

where $c = 1$.

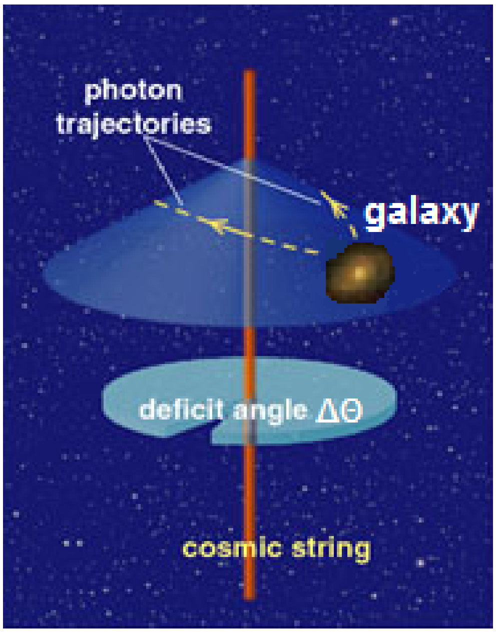

Figure 4.12: An illustration of the strong lensing by cosmic string. The space-time around the string can be obtained by removing the angular wedge of width $\Delta\Theta$, but remain flat everywhere. An observer can thus see double images objects located on a certain zone behind the string.

This is one of the most important astrophysical characteristic of a CS, because it defines the properties of the CS as gravitational lens [18], where μ is the linear density (or tension) of a cosmic string and G is the Newton constant. The physical properties of a CS predicted by Kibble are characterized by just one parameter, namely the mass per unit length μ, from which the lensing properties can be derived [26], [6], [8].

In gravitational lensing processes, the angular distance between lensed images depends on the deficit angle and from the linear distances (from the

observer to the lens and from the observer to the background source).
In general, this parameter also depends on the transverse velocity and orientation of the CS with respect to the observer. In fact, when the photons pass the cosmic string, they follow the geodesics of the conical space-time around the string and converge, acquiring an extra velocity component. However, in the simplified model derived here both effects can be safely neglected [19], [20]. The same result about deficit angle is obtained in a full relativistic analysis under the assumption of purely one-dimensional strings [6]. If the cosmic string has non-negligible width, then in general $\Delta\Theta > 8\pi G\mu$ [21]. However, in the case where $G\mu << 1$, Eq. (4.8) is a very good approximation.

In this work, I use the simplest kind of relation between the CS anisotropy δT, the CS mass per unit length μ and the projection β of the CS velocity on the plane perpendicular to the line of sight [18]:

$$\frac{\delta T}{T} = 8\pi G\mu \frac{\beta}{\sqrt{1-\beta^2}} \tag{4.9}$$

Here $T = 2.73K$ is the CMB temperature, δT has the order of μK, $c = 1$ is the speed of light.
We assume that the CS is far enough from the observer, so that the geometrical factor is close to 1 [3]. We also assume the CS perpendicular to the line of sight, so the CS velocity is equal to β (c=1). Finally, we use the relation between the CS tension μ and the observed angular distance $\Delta\Theta$ between two images of a remote galaxy lensed by CS, the deficit angle defined in (4.8). The peculiar form of the metric around a cosmic string can result in characteristic lensing patterns of distant light sources. In fact, the photons from a distant source travel in conical space-time and if a straight long string passes across our line of sight it may produce images which look as two exact copies of the same galaxy. This effect arises if the angular distance between the background galaxy and the CS in the plane perpendicular to the line of sight is smaller than CS deficit angle (proportional to the CS tension). In a more general case of loops and non-straight strings, the patterns will be more complicated, but still have a characteristic signature. The reason why we consider only straight string is simple, for astronomical constrains, these objects are much easier to detect than loops, for example. Furthermore, a a straight configuration for the string is energetically favourable, it will be more stable.

A CS signature can be found by searching for an excess of strong gravitational lensing events: the so-called chain or “Milky Way of gravitational

[3]The geometrical factor is defined as $\frac{R_g - R_s}{R_g}$ where R_s is the distance between the observer and the string and R_g is the distance between the source and the observer. We suppose that, on average, the CS is halfway between the source and the observer.

lenses" [6], Fig. 4.13.

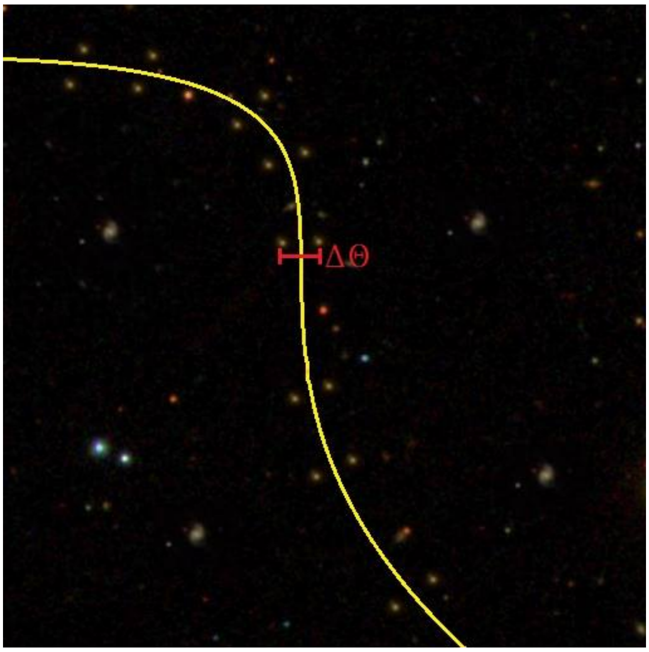

Figure 4.13: Merely figurative picture of cosmic string "Milky Way" [6]: a chain of background objects lensed by a cosmic string.

Since a cosmic string has a long structure, the light from all objects laying in the background within an angular distance from the string smaller than the deficit angle will be lensed. The final effect being that along the path of the string will appear a set of such pairs, rather than isolated pairs. The string, in fact, will lens all objects along its path, generating a linear excess (linear distribution) of lensed galaxies. In general, in wide-field astronomical images if there is a CS, we have to expect both ordinary gravitational lenses and lenses induced by the CS.

In our work, we focus on the case where gravitational lensing is caused primarily by galaxy-sized deflector in order to find an excess of candidate galaxies pairs. For low angular resolution, a pair of images of a source lensed by a CS looks like ordinary lensing. In the case of lensing of a galaxy by another galaxy or by some mass distribution, it is also appeared two images [22]. Therefore, there is the problem of distinguishing between normal lenses and lenses induced by a CS. This issue can be addressed statistically by using the observational estimations of the number of ordinary lenses at a given redshift and given magnitude. In the case of lensing by a CS, the surface brightness distribution presents discontinuities and strong gradients that are not present in ordinary gravitational lensing, where instead the resolved images could be distorted, forming arcs, but are otherwise smooth [22]. In fact, an important aspect of gravitational lensing by a cosmic string is that, at a difference with what happens for compact lenses, the images will be virtually undistorted due to the conical nature of the space-time. The only distortion which can arise are sharp edges in the fainter isophotes of an extended background source [18]. In other words, the isophotal analysis of lensed images could give the unambiguous proof of presence of a CS. However, if the two images have a large angular separation, the CS lensing features may be visible only in the outer faint isophotes and using high resolution instruments. Fig. 4.14 depicts a simulation of a galaxy lensed by a cosmic string [18].

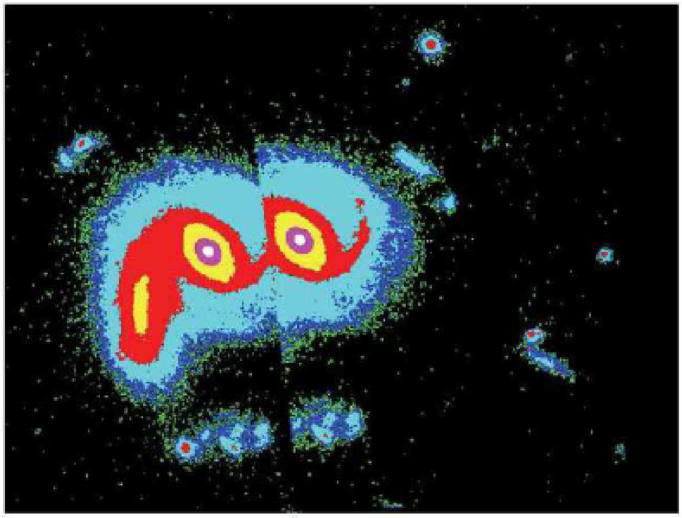

Figure 4.14: Example of gravitational lensing of a resolved galaxy by a cosmic string.

Furthermore, in contrast to what happens in other lensing models, the lensing by a cosmic string does not introduce any amplification of an individual image from the background source. It is worth recalling that it can not ruled out the possibility, even though rare, to face with a false positive case of two merging galaxies. Thereafter, we mention the resounding case of **CSL-1** [27].

An opportunity to detect the gravitational lensing signature by a cosmic string appeared in 2003, when the case of a peculiar object, named Capodimonte-Sternberg lens N.1 or CSL-1, was discovered in the OACDF [27], [28] but it had been rejected only at the end of a lengthy observational work, Fig. 4.15.

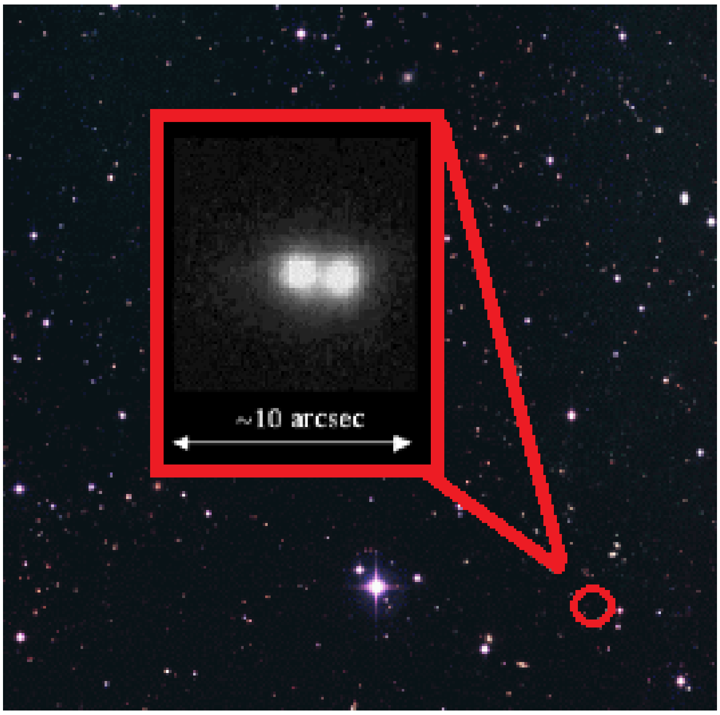

Figure 4.15: Capodimonte – Sternberg candidate lens n. 1, CSL-1.

CSL-1, located at $(\alpha, \delta) = (12:23:30.70, -12:38:57.8)$ is a double extended source laying in a low density field and with the two components separated by ~ 2 arcsec, so a separation compatible with the predictable deficit angle for a cosmic string. Both components are well resolved and have roundish and identical shapes in ground-based images. Low resolution spectroscopy showed that both components are at a redshift of 0.460 ± 0.008, while photometry (both global properties and luminosity profiles) matched those of giant elliptical galaxies at medium redshift. Visual inspection, comparison of main absorption lines, ratio of the spectra of the two components and their cross correlation, showed that the spectra of the two components, altough in the limited spectral range covered by the original spectra, were identical at a $\sim 99\%$ confidence level. These properties led to propose that this objects could be a background galaxy lensed by a cosmic string, and so the first case of gravitational lensing by a cosmic string.

A rare coincidental alignment of two identical giant ellipticals at the same redshift seemed very unlikely due to a series of odd conditions: the two ellipticals should have been relatively near $\approx 11kpc$ to each other, and in spite of this undistorted, with identical (within the errors) spectra, and residing in a relatively low-density environment (no other galaxies could be detected in the same region). The only method to clarify the nature of the object was to obtain high angular resolution images of the object (i.e. HST data), Fig. 4.16 [18].

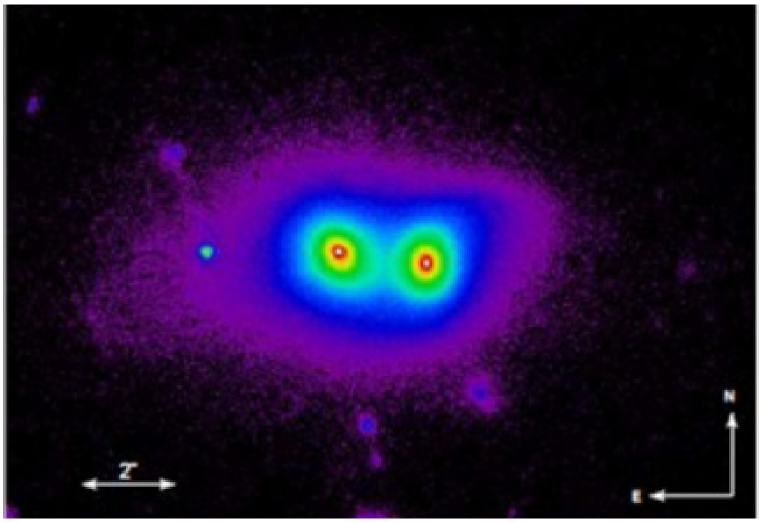

Figure 4.16: The actual HST image of CSL-1.

The simulations showed that lensing of an extended background object by a cosmic strings would introduce sharp edges in the low light level isophotes, but in average seeing conditions, these sharp edges are rounded off by the seeing and therefore not visible, Fig. 4.17 [18].

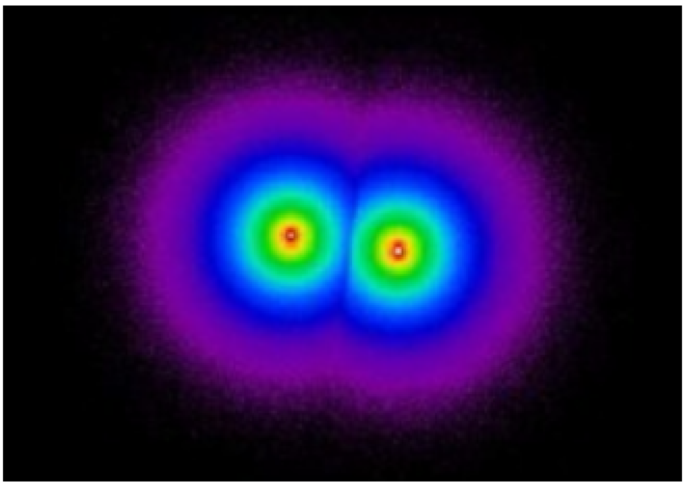

Figure 4.17: Numerical simulation of the image of an E galaxy as it would appear if lensed by cosmic string.

The follow-up high resolution analysis provided the interpretation of CSL-1 as two elliptical galaxies in an early state of interaction which may eventually lead to a merger, a rare case of "dry merger". Even though it was an unsuccessful case, the detailed study of this anomalous object allowed to determine which kind of observations are necessary to detect observational effects induced by cosmic strings [29], [30], [27], [19].

Since a high-resolution follow-up of many CS lens candidates is extremely time consuming, to persue this approach we first require a statistically significant indication of the presence of a CS. One possible approach is the use of an excess of gravitational lensing events in the region of the sky where recently we found traces of anisotropy by a CS, the gravitational lensing chain.

4.2.1 Feasibility test

To confirm the presence of a CS in the regions where we found CMB gradients, we looked for an excess of lensed galaxies pairs. We covered the area of $\sim \left((18.9^\circ)^2\right)$, assembled from 31 overlapping squared fields $1^\circ \times 1^\circ$ from $(\alpha = 11:29:03, \delta = +15:23:37)$ to $(\alpha = 10:57:47, \delta = +25:03:51)$. In the following, these fields will be called "string fields". Fig. 4.18 is an example of one of such fields with center $(\alpha, \delta) = (11:17:55, +18:52:27)$, from the STScI Digitized Sky Survey, POSS2/UKSTU.

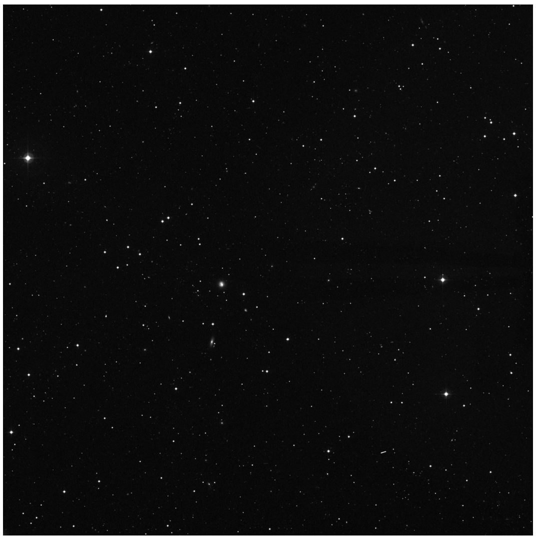

Figure 4.18: A $1^\circ \times 1^\circ$ string field with center $(\alpha, \delta) = (11:17:55, +18:52:27)$ in r-band from POSS2/UKSTU.

This field size is because of the resolution of 1° used for all sky radio data, but increasing a processing time or processing the selected areas instead of the whole sky, in future studies it will be possible to increase this resolution. In order to get these fields we used data from the STScI Digitized Sky Survey, POSS2/UKSTU [24], both for a preliminary visual analysis and when SDSS data were not available, and the same area is checked also using fields from Sloan Digital Sky Server DR12 [23], below we will provide the details.

- **The Sloan Digital Sky Survey**

  The Sloan Digital Sky Survey or SDSS is a digital imaging and spectroscopic survey of the high Galactic latitude sky, covering mainly in the Northern hemisphere.

  Images were taken using a photometric system of five filters (named u, g, r, i and z). These images are processed to produce lists of objects observed and various parameters, such as whether they seem pointlike or extended (as a galaxy might) and how the brightness on the CCDs relates to various kinds of astronomical magnitude. For imaging observations, the SDSS telescope used the drift scanning technique, which tracks the telescope along a great circle on the sky and continuously records small strips of the sky. The SDSS has taken deep images of more than one-third of the entire celestial sphere. It is possible to view SDSS images online for any object or sky position in the survey area, and download images of SDSS fields as FITS files. The SDSS data have been made available to the scientific community and the public in a roughly annual cumulative series of data releases. These data have been distributed in the form of direct access to raw and processed imaging and spectral files and also through a relational database, the "Catalog Archive Server", or "CAS", presenting the derived information.

  In this work we use photometric data from the Data Release 12 (DR12) that is the final data release of the SDSS-III, containing all SDSS observations through July 2014 to date. DR12 covers an area of $14,555$ square degrees and the total area of imaging (including overlaps) is of 31,637 square degrees. The following Figg. 4.19 and 4.20 show the area covered by the survey and the main features [17].

  Raw and processed image and spectroscopic data are available through the Science Archive Server, while the Catalog Archive Server provides the catalogs of photometric, spectroscopic, and derived quantities. More advanced and extensive querying capabilities are obtainable through "CasJobs", which allows time-consuming queries to be run in the background. The Imaging Query Form lets you search for catalog objects by position, magnitude, and other imaging constraints.

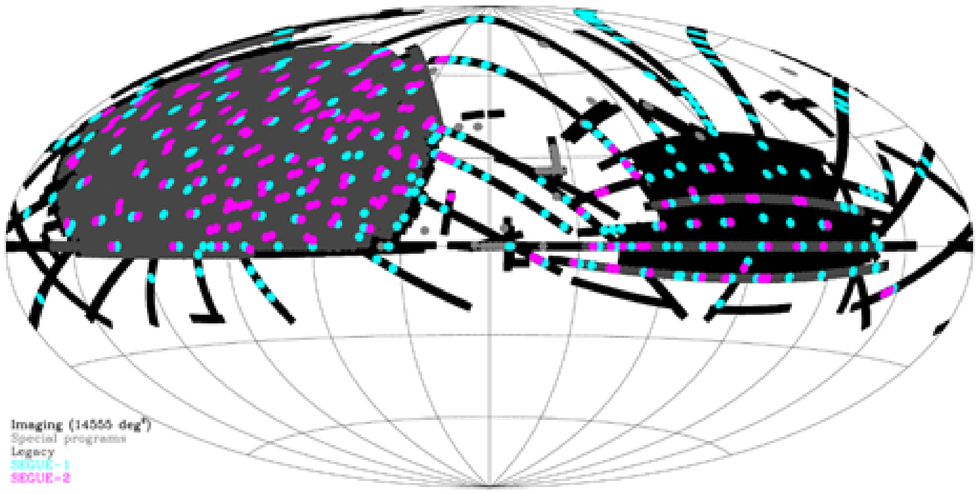

Figure 4.19: SDSS Legacy Sky Coverage.

Effective wavelengths & magnitude limits (95% completeness for point sources)
u 3551Å 22.0
g 4686Å 22.2
r 6165Å 22.2
i 7481Å 21.3
z 8931Å 20.5

Total unique area covered	14,555 square degrees
Total area of imaging (including overlaps)	31,637 square degrees (excluding supernova runs)
Individual image field size	1361×2048 pixels (0.0337 square degrees)
Number of individual fields	938,046 (excluding supernova runs)
Number of catalog objects	1,231,051,050
Number of unique detections	932,891,133
Median PSF FWHM, *r*-band	1.3 arcsec
Pixel scale	0.396 arcsec
Exposure time per band	53.9 sec
Time difference between observations of each band	71.72 sec (in *riuzg* order)
Global astrometric precision	0.1 arcsec rms (absolute)

Figure 4.20: Imaging statistics Data Release 12 (SDSS).

To build our sample we extracted from SDSS-DR12 all objects that are classified as "galaxy," whitin PhotoObjAll, the full photometric catalog quantities for SDSS imaging. So, we extract all galaxies together with their photometry; in particular we used the ("model _ Mag") magnitudes as they are fine for unresolved objects (at bright magnitudes, mag $<\sim 18$, model magnitudes may not be a robust means to select objects by flux), rejecting all objects with missing or non-detected in any of the SDSS photometric bands.
For the visual inspection, the quickest way to view SDSS imaging data for an area of sky is the SkyServer Navigate tool. It allows to navigate through sky images to look for interesting objects providing an interactive image of a given area of sky, with an overlay of catalog data for objects identified in that sky area. When you click on an object, the interface displays the main source properties. In this way it possible to get the information about the type of object, in particular for this work, the galaxies have been selected, the photometric redshift and the magnitudes in different bands.

- **The Second Palomar Observatory Sky Survey and the UK Schmidt Telescope Unit**

  The Catalogs and Surveys Group of the Space Telescope Science Institute has digitized the photographic Sky survey plates from the Palomar and UK Schmidt telescopes to produce the "Digitized Sky Survey" (DSS). The Second Palomar Observatory Sky Survey (POSS-II), conducted about 4 decades later, was the last of the major photographic sky surveys [25]. Using an improved telescope optics and improved photographic emulsions, it covered the entire Northern sky with ~ 900 partly overlapping $6.5°$ fields spaced by $5°$, in 3 bandpasses, corresponding to Kodak IIIa-J (blue), IIIa-F (red) and IV-N (far red) emulsions. The resolution depends on plate but typically it is $3''$. For this reason we decided to improve our analysis using SDSS catalog.
  When retrieving images from the MAST site this is the mapping between available survey options and the individual surveys: for all fields, string and control ones, we use the surveys POSS2/UKSTU Red and POSS2/UKSTU Blue. By entering a height and width in arcminutes, we specify the field size of $1° \times 1°$ for the returned image.

Before embarking in our analysis, the question we want to address is: can strong lensing events by cosmic strings be observed and used as a way of demostrating the presence of a CS? So, we calculate the expected number of objects, in particular galaxies, which a straight string would lens in an average ordinary extragalactic field. With the word "ordinary field" we indicate a region of the sky where there is no indication (from CMB maps) of the presence of a string. These fields will be used both to measure the average density of objects in the sky as well as "control fields" in order to verify the presence of an excess of lens candidates. We choose eleven control fields all around the string region. They cover an area of $\left((\sim 12.6°)^2\right)$, that we have calculated using the procedure described in Appendix A.
To this end we submit to SDSS SkyServer a query to download a catalog of all galaxies within the region of interest. So, using SDSS data we producing a preliminary catalog, setting the following criteria:

- we choose all objects identified as "Galaxy": we want all pairs made of two galaxies rejecting the false positive, i.e. star-galaxy, star-star, etc. which are not the case of CS. We exclude objects like stars because we are interested to strong gravitational lensing, that need two things (1) the lens must be very massive to produce a big enough image to see and (2) the alignment needs to be just right i.e. the object must be almost exactly behind the lens;

- we choose all objects having a measured photometric redshift with its error;

- we choose all objects having a measured Model_ mag [4] in all five bands (u, g, r, i and z) with their error;

- we require all objects having extension, i.e. *petrorad* [5], between 0.1 e 4.5 arcseconds. The lower limit is an indicative value because we want extended objects but not extended more than the deficit angle, whose

[4] Just as the PSF magnitudes are optimal measures of the fluxes of stars, the optimal measure of the flux of a galaxy would use a matched galaxy model. With this in mind, the code fits two models to the two-dimensional image of each object in each band:

1. a pure deVaucouleurs profile,
2. a pure exponential profile.

The best-fit model in the r-band is fit to the other four bands; the results are stored as the model magnitudes.

[5] The Petrosian radius r_P is defined as the radius at which $R_P(r_P)$, ratio of the local surface brightness in an annulus at r to the mean surface brightness within r, equals some specified value $R_{P,lim}$.

maximum value in our analysis is $9''$. For this reason, we fixed the upper limit as the half of $\Delta\Theta$.

The query returned a total number N of 138556 objects over $\left((12.6^\circ)^2\right)$ for the control fields:

Control field number	*Objects from catalog*	*1σ level objects*
1	11858	20
2	12635	16
3	13689	23
4	14522	29
5	13252	27
6	16522	32
7	16079	31
8	15691	20
9	2341	4
10	9492	12
11	12475	15

Table 4.2: Results of automatic algorithm for 11 control fields of area $\left((12.6^\circ)^2\right)$. In the second column all objects from catalog for each control field, in the third column the candidate pairs that satisfy the photometric criteria at 1σ confidence level.

To calculate the total number of galaxies that a string can lens, we must first set limits on the magnitude of the objects for each band, because we confine our search to objects that we can inspect by eyes. Each limit value corresponds to the minimum magnitude of candidate lens pair obtained with visual inspection of two control fields, $CF_1 = (10:56:16, +15:47:35)$ and $CF_2 = (11:06:50, +13:25:36)$, Table 4.3:

Band	*Model_mag limit*
u	24.6
g	24.2
r	23.0
i	22.2
z	22.3

Table 4.3: Magnitude limits in all five bands.

We incorporate the information we get into the above criteria obtaining, for eleven ordinary fields, the total number of galaxies $N_{tot} = 76659$. Knowing this quantities, we can divide over all control field area $\left((12.6°)^2\right)$ to obtain the mean value of N_{tot} for square degree of area , $\overline{N}$:

$$\overline{N} \pm \sqrt{\overline{N}} \simeq 6084 \pm 78 \tag{4.10}$$

Since we assume that lensed galaxies have maximum separation of $9''$, fixing a small region of $1° \times 9''$ $\left((0.0025°)^2\right)$ as $a)$ in Fig. 4.21, the number of galaxies in it is

$$N^{perp}_{expected\ lens} = 15.2 \pm 3.9 \tag{4.11}$$

or if we consider the situation $b)$ in Fig. 4.21.:

$$N^{obl}_{expected\ lens} = 21.5 \pm 4.6. \tag{4.12}$$

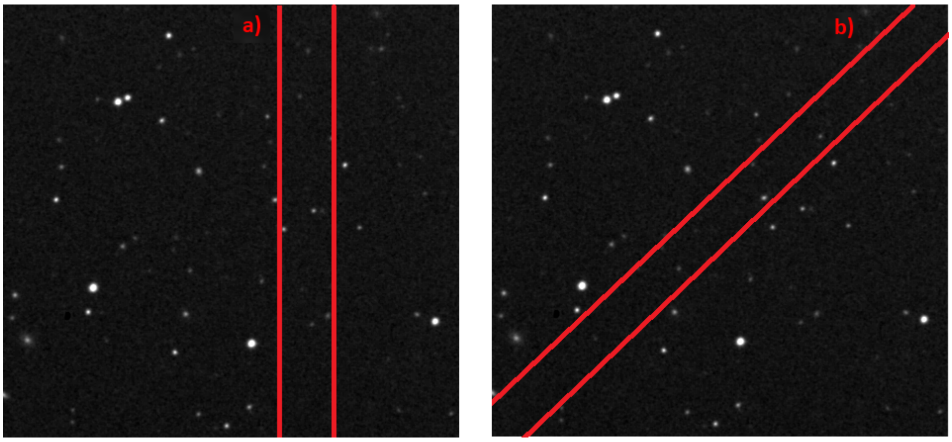

Figure 4.21: Two different cases for a straight cosmic string to across the sky in a region of maximum width $9''$.

What has just been calculated, are only lower limits to the expected number of lensed galaxies as we are assuming that the string is locally straight and the field that we took in account is not surely affected by gravitational effect due to the string, according the processed CMB radio maps.

At this point, it is fundamental to understand if it is possible to measure the excess of lensed galaxies with respect to false positive pairs, like galaxies pairs due to gravitational lensing not by a cosmic string or simply galaxies close in projection on the sky, as in the case of CSL-1. We process the catalogs of the control fields applying with the software TOPCAT, an interactive graphical viewer and editor for tabular data. The aim is using an algorithm to estimate the statistical significance of the excess of candidate galaxies pairs produced by strong gravitational lensing due to the CS. So after matching, separately, each catalog with itself to obtained pairs, we adopt the following criteria:

1. we choose the pairs separated by angular distance $2'' < \Delta\Theta < 9''$. This range come from taking into account as lower limit the resolution of the survey and for the upper limit the relation (4.8), i.e. we are searching for close objects pairs in according to the tension $10^{-7} < \mu < 10^{-6}$ [6] for an individual cosmic string [6];

2. we fix magnitude limits in each bands, as reported in Table 4.3;

3. we evaluate the redshift of each component of the pair: these have to be equal (within the error) for gravitational lens systems;

4. we evaluate the colors of each component of the pair: these have to be equal (within the error) in all the SDSS Survey bands (u, g, r, i, z) [23]; in fact the gravitational lensing gives an acromathic effect: the intensity can change but not the color of light rays.

The last two conditions 3. and 4. traslate in:

$$\left|\left(m_x^1 - m_x^2\right) - \left(m_y^1 - m_y^2\right)\right| = k \cdot \sqrt{(\Delta_{m_x})^2 + (\Delta_{m_y})^2} \tag{4.13}$$

with

$$\Delta_{m_x} = \sqrt{(e_x^1)^2 + (e_x^2)^2} \tag{4.14}$$

where $m_x^1, m_x^2, m_y^1, m_y^2$ are the magnitudes for two galaxies in one pair in the bands x and y respectively, $e_x^1, e_x^2, e_y^1, e_y^2$ are the 1σ error bars for definition of each magnitude.

Similarily:

$$z_1 - z_2 = k \cdot \sqrt{e_{z_1}^2 + e_{z_2}^2} \tag{4.15}$$

where $e_{z_1}^2$ and $e_{z_2}^2$ are the redshift errors of the two pair objects and $k = 1, 2, 3$ is the significance threshold that we decide to adopt. In present analysis, we let us just consider the 1σ significance level.

The procedure leads to a list of 229 pairs ($N_{backgoround\ tot}$) for all ordinary fields. Fig. 4.22 shows an example of the distribution of the pairs in one of our control fields.

[6] We report the formula used to derive the limits: $\Delta\Theta = 8\pi \frac{\mu}{m_{Planck}^2}$, where m_{Planck} is the Planck mass defined as $m_{Planck} = \sqrt{\frac{\hbar c}{G}}$. In our case $\hbar = c = 1$.

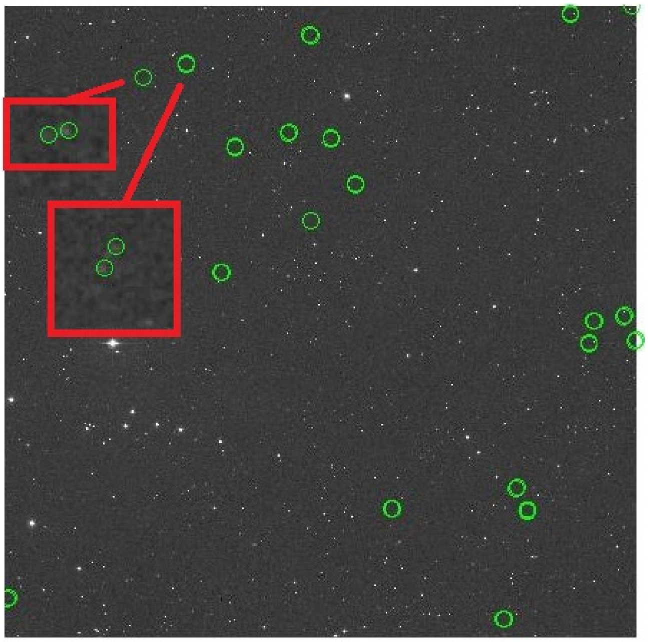

Figure 4.22: Control field N.1, where the green circles mark the positions of candidate lensed pairs.

Thus, in an average field of $1° \times 1°$, we compute $N_{background}$ as follows:

$$N_{background} = \frac{N_{backgoround\ tot}}{Area_{CF}} = 18.17 \tag{4.16}$$

Now, we can calculate the signal to noise ratio to know the significance of the expected excess of pairs (always considering a 1 square degree field) as:

$$\frac{S}{N} = \frac{N_{expected\ lens}}{\sqrt{N_{expected\,lens} + N_{background} \times 2}} \simeq 2.6 \tag{4.17}$$

What we have achieved justifies and validates our experiment. In fact, this successful result demonstrates that, using our data, is possible to detected the presence of cosmic strings at 2.6σ confidence level. Furthermore, the feasibility test is conducted considering only a $1° \times 1°$ field. Since we use a total area of $\left((12.6°)^2\right)$, we can produce better results than the previous of a factor $\sim \sqrt{12} > 3$, thereby improving our experiment.
It is important to stress that the two catalogues of galaxy pairs include either resolved (i.e. extended) objects or pairs that are not as readily recognizable as string-lensed pairs, due to their faintness. A forthcoming investigation will be devoted to search for discontinuities in the outer isophotes of the resolved lens candidates.

4.2.2 Optical analysis of galaxy pairs in the CSc-1 field

The same above procedure is also applied to string fields, Table 4.4.

String field number	*Objects from catalog*	1σ *level pairs*
1	16969	25
2	16596	13
3	14319	18
4	12481	12
5	12280	12
6	11937	11
7	12036	7
8	11766	25
9	12423	14
10	11556	5
11	12549	14
12	13090	17
13	13940	19
14	15251	14
15	14726	21
16	16491	14
17	16035	11
18	14527	13
19	13731	13
20	14087	7
21	14507	10
22	14184	15
23	14012	14
24	13429	8
25	13188	5
26	13787	12
27	15025	8
28	15628	12
29	14656	23
30	13476	17
31	14030	18

Table 4.4: Results of automatic algorithm for 31 string fields of area $\left((18.9°)^2\right)$. In the second column all objects from catalog for each control field, in the third column the candidate pairs that satisfy the photometric criteria at 1σ confidence level.

We obtain a total number of 427 pairs ($N_{pairs\ tot}$) in the total area of $\left((18.9^\circ)^2\right)$ of string fields that satisfy all above-cited photometric criteria.

The mean number of galaxies pairs per square degree in a string field is:

$$N_{pairs} = \frac{N_{pairs\ tot}}{Area_{SF}} = 22.59 \tag{4.18}$$

Now, we have all elements to calculate the number of objects in excess respect to the number of background objects:

$$N_{excess} = N_{pairs\ tot} - N_{background\ tot} \cdot \frac{Area_{SF}}{Area_{CF}} = 82.5 \tag{4.19}$$

so, we have an excess of 4.36 pairs per square degree. The error of the excess is:

$$\Delta N_{excess} = \sqrt{N_{pairs\ tot} + N_{background\ tot} \cdot \left(\frac{Area_{SF}}{Area_{CF}}\right)^2} \simeq 30.7. \tag{4.20}$$

The significance is:

$$\frac{S}{N} = \frac{N_{excess}}{\Delta N_{excess}} = 2.7. \tag{4.21}$$

Hence, current result seems to suggest that there is a small excess of about 20% in a one square degree string field respect to the same area control field. This result is in full agreement with the expected result of cosmic strings scenario: in the presence of a cosmic string should be an excess of the gravitational lensing events.

In order to identify if there is a preferred range of separation between the components of pair, we compare the distribution for ordinary fields and string fields, after rescaling the number of pairs at same area. Fig. 4.23 is what we obtain: there is an excess of $\sim 38\%$ of pairs in the string fields in the range $[8'', 9'']$. It should be a first indication of the physical properties of the cosmic string.

As discussed before, we can reasonably assume that the string is straight, so we can find its direction by checking if there is a preferred orientation between close pairs of galaxies along straight lines across the sky. For each field, we calculate the relative number of pairs with the same angle of inclination β as a function of PSF. Let us give a description of the search methodology. For a line l which connects the centers of the pair components (with the specified coordinates $\{x_1, y_1\}$ and $\{x_2, y_2\}$ for the 1^{st} and 2^{nd} component, respectively), we can write the equation of the perpendicular line l_p in the form:

$$y = -\frac{(x_2 - x_1)}{y_2 - y_1} \cdot x + \frac{(x_2 - x_1)}{y_2 - y_1} \cdot x_1 + y_1 \tag{4.22}$$

The accuracy (or the error) $\Delta\beta$ on the slope of the line l_p is defined by the PSF of nearest star from the equation:

$$\left(\frac{FWHM}{\Delta\Theta}\right) = tg\left(\frac{\Delta\beta}{2}\right), \tag{4.23}$$

where $\Delta\Theta$ is the angular distance between pair components and FWHM (full width at half-maximum) is the angular resolution of the survey. In spherical coordinates

$$\Delta\Theta = \sqrt{(y_1 - y_2)^2 + cos^2 y_1 \cdot (x_1 - x_2)^2}. \tag{4.24}$$

The inclination angle β_i (in arcsec) for each pair i, and its error are given by:

$$\beta_i = -arctan\left(\frac{x_{i2} - x_{i1}}{y_{i2} - y_{i1}}\right) \pm \Delta\beta \tag{4.25}$$

where

$$\Delta\beta = 2 \arctan\left(\frac{PSF_i}{\sqrt{(y_{i1} - y_{i2})^2 + \cos^2 y_{i1} \cdot (x_{i1} - x_{i2})^2}}\right). \tag{4.26}$$

For each pair we found in the string and in the control fields, in order to estimate the number of pairs which have compatible orientation, we calculate the corresponding angle β and its error $\Delta\beta$. This error is related, as you can see in the formula (4.26), to PSF value. We choose three different cases for $\Delta\beta$: the ideal case of $\Delta\beta = 0$, $\Delta\beta$ with $PSF = 1.185''$ (this value has been calculated from the reference star in one of the string fields), and $\Delta\beta$ with $PSF = 1.3''$ (it is the median PSF FWHM in r-band declared in the SDSS catalogs). According to the theory, we expect the random uniform distribution of β_i in fields without the CS and a multi-modal distribution or a distribution with a single peak in the fields with a CS candidate.

The reason of such a “multi-modality” depends on the curvature of the string. In the simplest case of a straight string, if the gravitational lensing pairs are formed by a string, the angles of the lines l should obviously be the same. In a more realistic case, when the string admits a curvature line, however, one have to expect the number of pairs with certain angles of inclination should overcome the number of pairs with other angles.

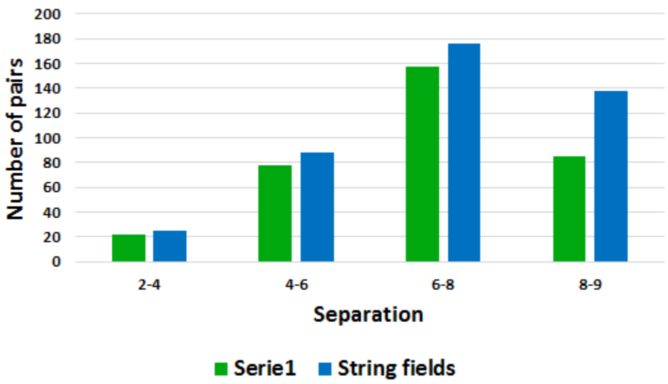

Figure 4.23: The histogram for different separation of the pairs for string (blue bar) and ordinary fields (green bar). It is possible to see the greatest excess for separation $[8'', 9'']$.

In the search procedure of the pairs, we considered a rather wide window for possible distances between the pair components, from $2''$ up to $9''$. For the purpose to search such an excess for a certain angle we divided the interval $2'' - 9''$ into four subintervals: $[2'', 4'']$, $[4'', 6'']$, $[6'', 8'']$, $[8'', 9'']$. For each of the subintervals we plot the following histogram: the x-axis shows the intervals of inclination angle β of the line l (binned in $10°$ intervals: $\beta \in ([170°, 180°], [160°, 170°], ...[0°, 10°]))$, the y-axis shows the numbers of pairs n. This histogram is done for β without its error $\Delta\beta$, see Figg. 4.24, 4.25.

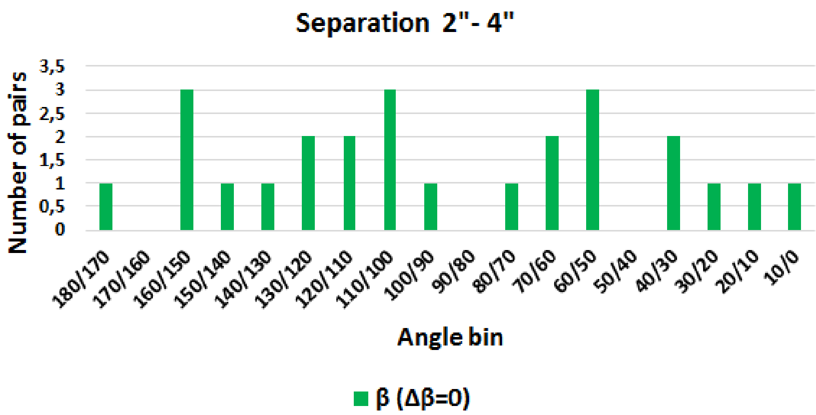

Figure 4.24: The histogram for the pairs with separation $[2'', 4'']$ for string fields. The green bars represent β with $\Delta\beta = 0$. The angle bin is in $[°]$.

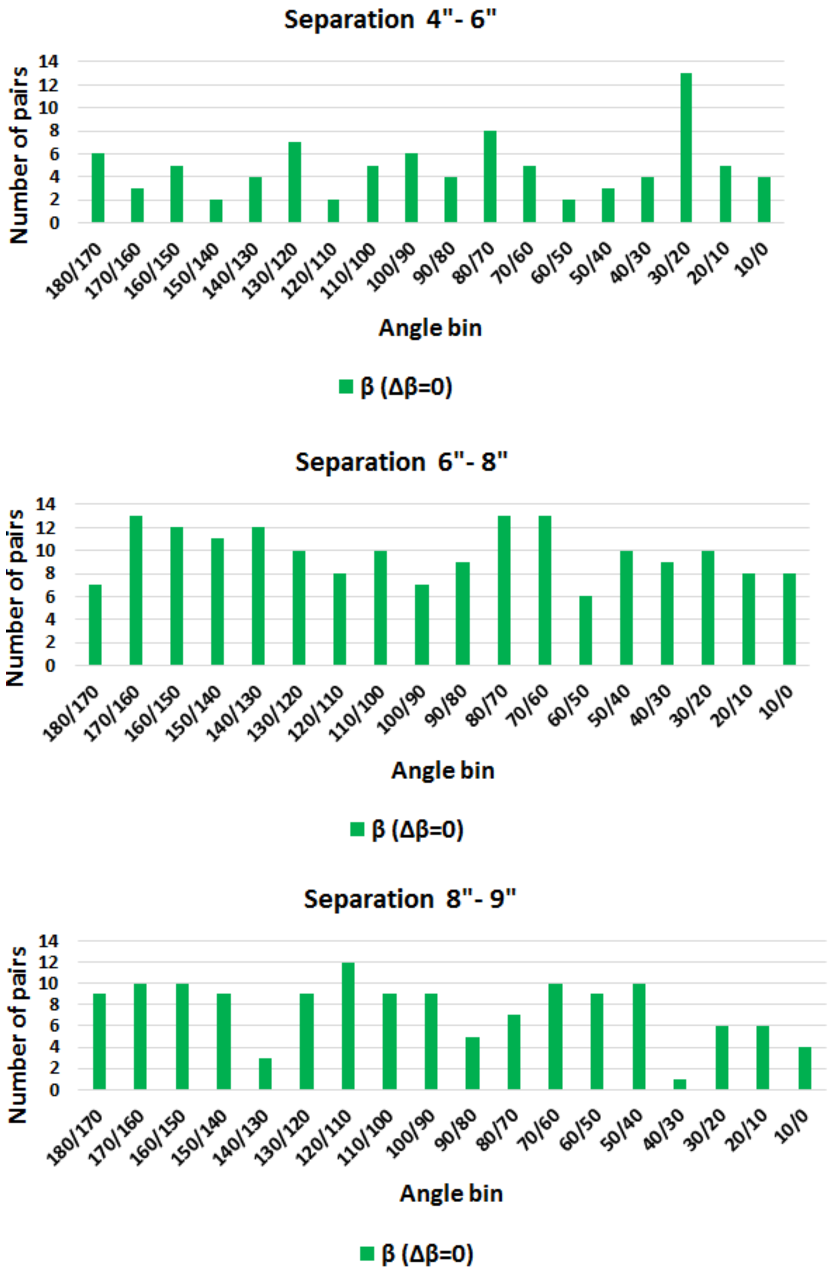

Figure 4.25: The histograms for different separation ($[4'', 6'']$, $[6'', 8'']$, $[8'', 9'']$) of the pairs for string fields. The green bars represent β with $\Delta\beta = 0$. The angle bin is in $[^\circ]$.

We apply **Student's t-statistics** to test the presence of an excess in the distribution of pairs numbers for a certain inclination angle interval, after checking with the χ^2-test the normal distribution of our samples. For each subinterval ($[2'', 4'']$, $[4'', 6'']$, $[6'', 8'']$, $[8'', 9'']$) we calculated the mean and s.d. values as

$$\mu_k = \frac{1}{18}\sum_{i=1}^{18} n_{ki},$$

$$\sigma_k = \sqrt{\frac{1}{18-1}\sum_{i=1}^{18}(n_{ki} - \mu_k)}.$$

where $k = 1, 2, 3, 4$ and n_{ik} are the number of pairs for each interval of inclination angle β. For each maximum value n^*_{ki}, if

$$\frac{|n^*_{ki} - \mu_k|}{\sigma_k} > t(5\%, 18-1)$$

then we have a surplus for significance level 5%. Here, $t(5\%, 17) = 2.11$ is the table value of the Student's t-statistics which depends on the significance level and the number of degrees of freedom, $DF = 17$.

The results are the following:

1. For the subinterval $[2'', 4'']$ the excess in pairs number is 10% (in comparison with mean value of ordinary fields) and $t-$statistics is $t_{5\%} = 1.641 < 2.11$. No excess at any β.

2. For the subinterval $[4'', 6'']$ the excess in pairs number is 12% (in comparison with mean value of ordinary fields) and $t-$statistics is $t_{5\%} = 3.082 > 2.11$. This excess is for $\beta \in [20°, 30°]$.

3. For the subinterval $[6'', 8'']$ the excess in pairs number is 11% (in comparison with mean value of ordinary fields) and $t_{5\%} = 1.457 < 2.11$. No excess at any β.

4. For the subinterval $[8'', 9'']$ the excess in pairs number is 38% (in comparison with mean value of ordinary fields) and $t_{5\%} = 1.489 < 2.11$. No excess at any β.

It indicates the statistically significant abundance of $[4'', 6'']$ distanced pairs in the interval $\beta \in [20°, 30°]$ in equatorial system, that corresponds in galactic system to $\beta \in [10°, 21°]$ (in the Appendix B the calculation of the string inclination angle β from the equatorial system to the galactic system is reported). Although the excess of pairs in the string fields respect to the ordinary fields pairs in that case is 12% we cannot overlook this result without further check. In more realistic cases, when we consider the $\Delta\beta$ is more difficult to identify an overshoot, the difference becomes statistical equivalent. To establish the reliable correlation with the presence of a cosmic string it is needed optical observations with higher precision.

In addition, for the $[4'', 6'']$ interval, according to the physical meaning of the data (we have positive and integer values of number of galaxies pairs with different separation between the components for each of β angle bin), let us assume the **Poisson distribution** of the pairs in each β angle bin. We also assume that the Poisson distribution is the same for all angle bin and thus, we can take λ as the average value of the occurrences over all angle bins. The probability density of having x occurrences within a given interval is:

$$f(x) = \frac{\lambda^x e^{-\lambda}}{x!}.$$

Table 4.5 reports the results of the statistic, considering the value in the upper tail of the function $f(x)$, P.

$Separation$	λ	x	P
$[2'', 4'']$	1.389	3	0.0525
$[4'', 6'']$	4.889	13	0.00056
$[6'', 8'']$	9.778	13	0.120
$[8'', 9'']$	7.667	12	0.049

Table 4.5: The results for the Poisson's distribution test. For each separation interval, λ is the average number of pairs, x is the excess and P the The probability of observing x pairs per interval.

It is clear that the excess, that we have already found using t-Student test, is again confirmed by this different test. In fact, the probability that n=13 for the subinterval $[4'', 6'']$ is too low, indicating that it is an anomalous value.

A further check for the excess of $[4'', 6'']$ distanced pairs comes by considering the orientation angle ϕ of these pairs respect to the equatorial plane. If we consider a $x - y$ reference frame, we define "orientation angle" the angle of the line joining the centres of galaxies of each pair forms with the x-axis (in other words, respect to the Equator). According to theoretical predictions, if the temperature gradient on radio maps is a signature of the presence of a cosmic string, since we selected fields along that gradient, we expect to find galaxies pairs oriented orthogonally to the string fields direction. In order to verify this hypothesis, we plot the centres of string fields (blue dots) and the centres of the pairs in excess (orange dot) as showed in Fig. 4.26.

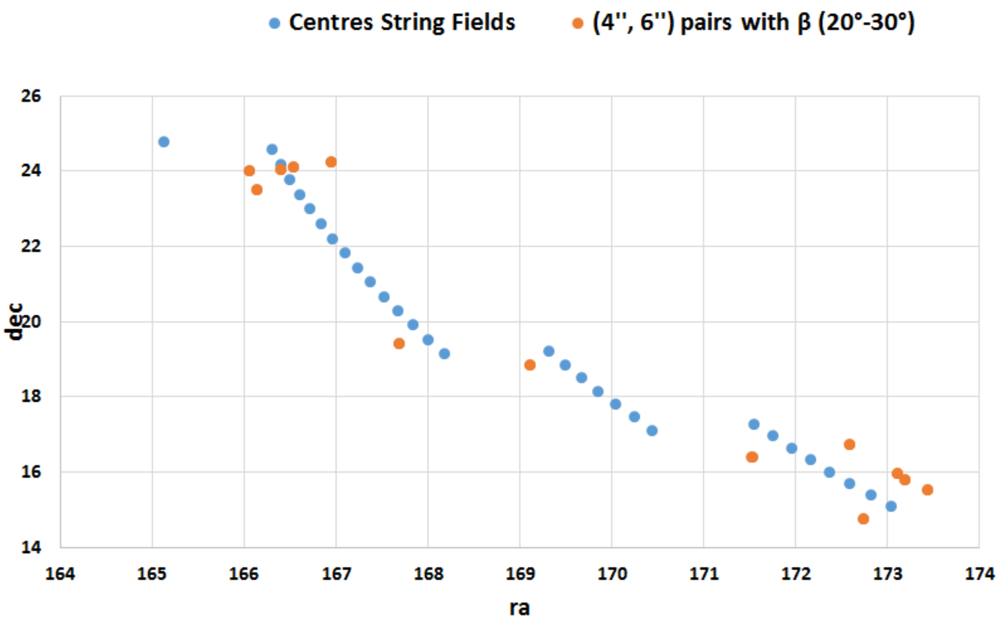

Figure 4.26: The position in the sky (in equatorial system) of the centres of the string fields (blu dot) and the centres of the galaxies pairs distances $[4'', 6'']$ with $\beta \in [20°, 30°]$. The coordinates are in decimal degrees.

Let us look at the orientation of the pairs and the string fields, calculating their orientation angle ϕ, reported in the following Tables 4.6 and 4.7:

α_1	δ_1	α_2	δ_2	ϕ
11 : 33 : 42	+15 : 32 : 51	11 : 33 : 41	+15 : 32 : 47	66
11 : 30 : 53	+14 : 47 : 19	11 : 30 : 53	+14 : 47 : 14	61.3
11 : 32 : 42	+15 : 49 : 21	11 : 32 : 42	+15 : 49 : 17	69.8
11 : 32 : 22	+16 : 00 : 09	11 : 32 : 22	+16 : 00 : 14	62.8
11 : 30 : 18	+16 : 45 : 58	11 : 30 : 19	+16 : 46 : 01	66.3
11 : 26 : 03	+16 : 24 : 36	11 : 26 : 03	+16 : 24 : 31	60.5

Table 4.6: The coordinates of each galaxy of pairs (α_1, δ_1) and (α_2, δ_2) (in equatorial system) and the orientation angle ϕ. The mean value of ϕ is $\bar{\phi} = 64.4$.

α	δ	ϕ
11 : 32 : 08	+15 : 07 : 04	−53.1
11 : 31 : 13	+15 : 25 : 09	−53.9
11 : 30 : 19	+15 : 43 : 38	−54.8
11 : 29 : 27	+16 : 02 : 17	−55.6
11 : 28 : 36	+16 : 21 : 05	−56.5
11 : 27 : 45	+16 : 40 : 06	−57.2
11 : 26 : 56	+16 : 59 : 12	−58.2

Table 4.7: The coordinates of the centres of string fields (α, δ) (in equatorial system) and the orientation angle ϕ. The mean value of ϕ is $\bar{\phi} = -55.6$. The sign minus is because the angle we measure goes clock-wise.

Fig. 4.27 below shows the orientation in the sky of the centers of the galaxies pairs and the centers of string fields.

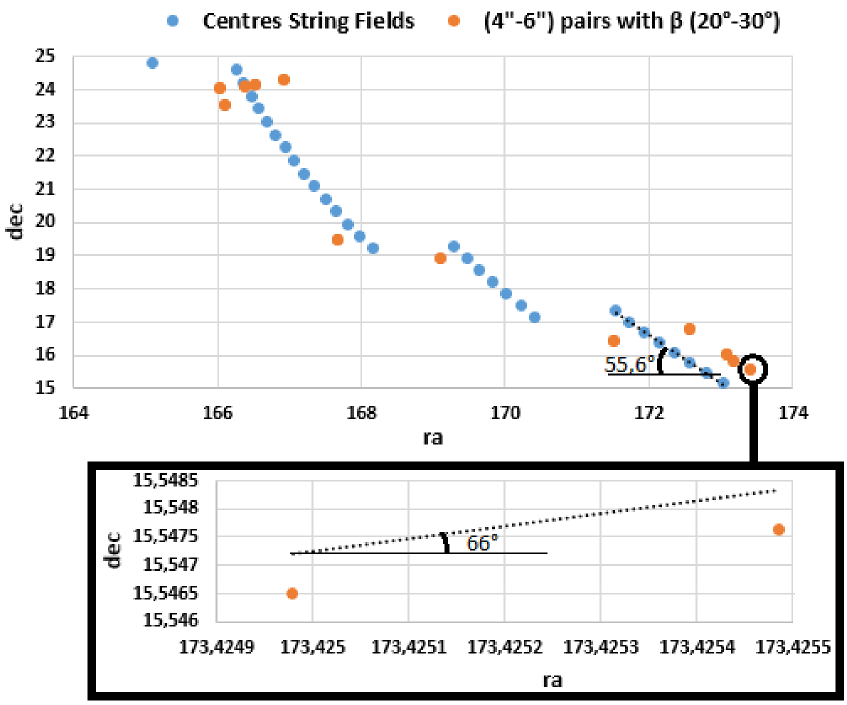

Figure 4.27: The position in the sky (in equatorial system) of the centres of string fields (blu dots) and the centres of the galaxies pairs distances $[4'', 6'']$ with $\beta \in [20°, 30°]$ (orange dots). In the upper panel the dashed line is the best fit of the last seven centers of string field with orientation angle equal to $-55,63°$; in the lower panel the pair with coordinates $(11:33:42, +15:32:51)$ and $(11:33:41, +15:32:47)$ with orientation angle $66°$. The coordinates are in decimal degrees.

The result is that the each other's position between the pairs and the fields is almost orthogonal in the sky: this seems to suggest that there is the possibility that the galaxies pairs are lensed by a string that should pass in the middle of them. If we take in account the error $\Delta\beta$, that in the case of $PSF = 1.3''$ has as mean value $27.5°$ and the not so high resolution of the radio maps ($1°$) from which has been selected the region of the cosmic string candidate, there is a reasonable agreement between the orientation of galaxies pairs and string fields. The nature of these pairs should be confirmed by high resolution observations (similar to CSL-1) in order to remove false positive pairs and obtain a definitive conclusion.

In carrying out this study, it has been also necessary to proceed with the visual inspection to check the quality of the automatic algorithm in order to improve the selection of the galaxies pairs. For this purpose we used the Sloan Digital Sky Server DR12, to verify the candidates using 5 bands with resolution $1.3''$. Fig. 4.28, in the next page, shows some examples of candidates lens galaxies pairs for different deficit angles found via automatic procedure and then they are checked on SDSS DR12 Navigate Tool.

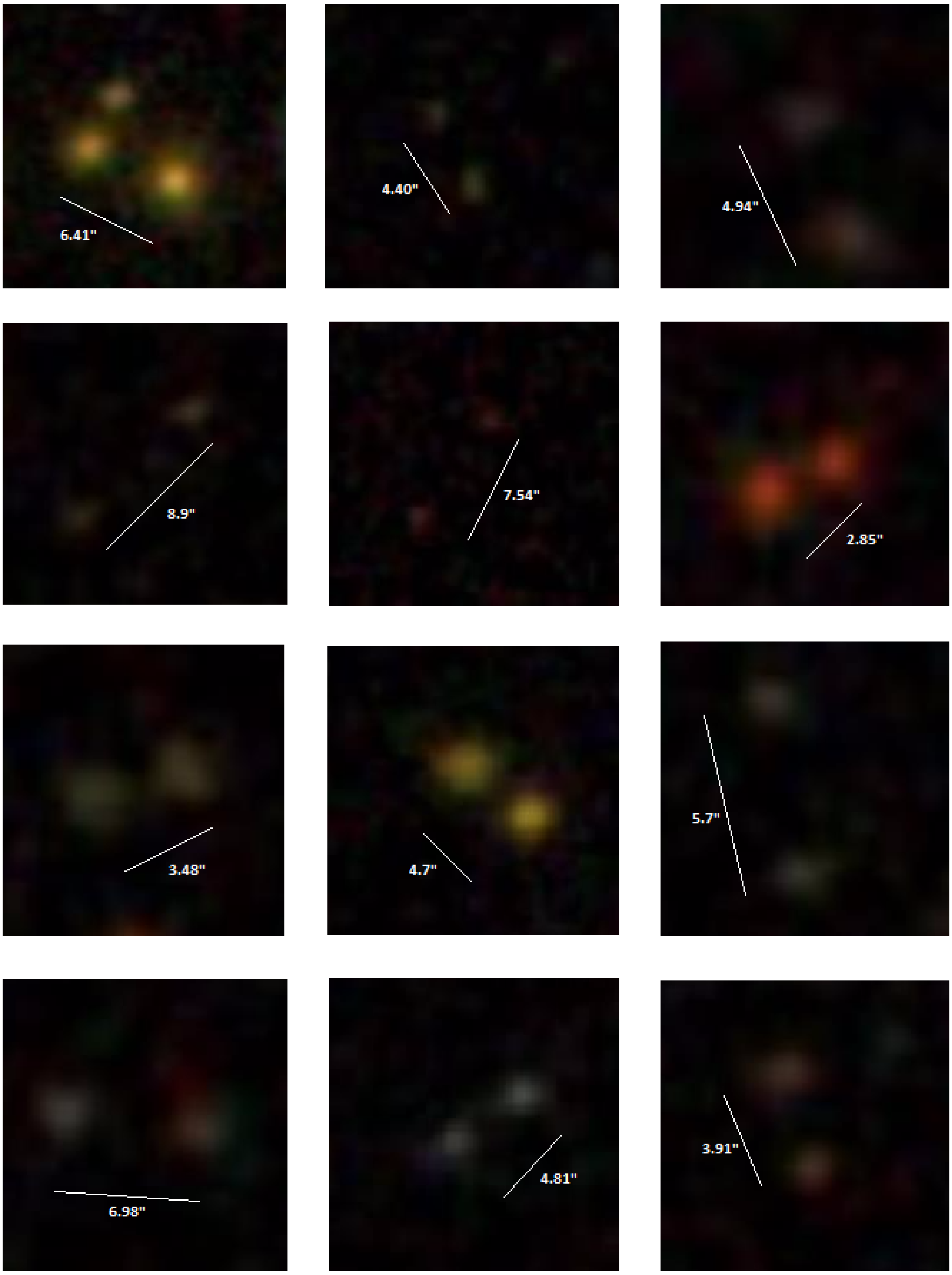

Figure 4.28: Candidate lens galaxies pairs from SDSS DR12. The white line indicates the separation between the two components of the pair.

Chapter 5

Results and conclusions

Cosmic strings are expected to produce well defined and unambiguous observational features. In the CMB radiation, cosmic strings produce well defined step-like discontinuities. In the CMB maps the anisotropy induced by a cosmic string would appear as a sequence of zones of decreased and increased temperature: first a cold spot in front of the moving string, then a step-like jump followed by an hot spot and, finally, a second cold spot [36]. In fact the structure of such temperature fluctuation is dependent on the cosmic string parameters since they are affected by the position of the string with respect to the observer, by the string velocity and direction, and by the string linear density. In optical surveys the indication of the presence of a cosmic string is a chain of lensed galaxies and sharp edges in well resolved galactic images.

In this thesis, we addressed the problem of recognition of the cosmic strings signatures using both radio data and optical one. In the first part, the elaborated and tested algorithm to CS detection in CMB maps from WMAP and Planck mission was applied to identify cosmic strings candidates. This algorithm is based on convolution procedure of original observational radio data with modified Haar functions (MHF) and it is able to achieve the resolution for CS deficit angles of the order of 1 arcsec. The main result that there are no CS with tension larger than $G\mu/c^2 = 7.36 \times 10^{-7}$. Secondly, we found a list of preliminary CS candidates in the Planck data, after fixing two main necessary conditions to handle found structures as CS candidates. In particular, we selected the best candidate (CSc-1) in order to carry on the subsequent optical analysis, identifying its position in the sky. The same CS candidates have been found in the WMAP 9-year data. Finally, our MHF algorithm with the results in [2] made it possible to clarify the preferred CS types. The most preferable types of CS are semilocal strings. They can have ends (monopoles) and can be unstable under certain conditions. They can be closer to us, being not very long. The structure of the CS candidates found by the MHF method confirms the view of semilocal CS as a collection of segments. Therefore, our strategy has been to find suitable optical fields to search for the chains of gravitational lenses, produced by candidates semilocal CS. Independence of Planck and WMAP data sets serves as an additional argument to consider those CS candidates as very promising.

In the second part, we considered simple model of a long straight CS moving in the plane perdendicular to the line of sight and that it is far enough from the observer. The convolution of radio maps, obtained from WMAP and Planck CMB data, provides a list of preliminary CS candidates with amplitude $\delta T/T \lesssim 40\mu K$. After selecting the best one (CSc-1) covering the field of area $\left((18.9^\circ)^2\right)$, we carried on the optical analysis, based on the search of sources of strong gravitational lensing.
First of all, we computed the possibility to detect an excess of candidate lens pairs in the ordinary fields and then we measured the excess of lensed galaxies with respect to false positive pairs. As result we attested the feasibility of our experiment at 2.6σ level of confidence to detect the presence of a cosmic string. Using a simple algorithm, we identified lens candidates that satisfy photometric criteria and we obtained a list of 427 pairs in the total area of string fields and 229 pairs for all ordinary fields. The conclusion is that the number of gravitational lensing candidates we found in string fields is 20% greater as in the ordinary fields and this result is in full agreement with the cosmic strings scenario. Assuming pure Poissonian fluctuations this excess is significant at the 2.7σ level.
The next step was to find, assuming that the string is straight, its orientation by correlating close pairs of galaxies along the string. We plotted all angle β without its error (the simplest case) in order to estimate the relative number of pairs which have compatible orientation. Taking in account the different possible distances between the pair component, we found the dominant direction of the arrangement of pairs for $[8'', 9'']$ angular separations. In order to ascertain the presence of an excess in the distribution of pair numbers for a certain inclination angle interval, we plotted, separately for each separation intervals, the number of pairs of different intervals of inclination angle β. Then we applied Student's t-statistics, getting as result for the first test a statistically significant excess of $[4'', 6'']$ distanced pairs in the interval $\beta \in [20^\circ, 30^\circ]$. This result is also confirmed by the Poisson's test. Although

the excess of pairs in the string fields respect to the ordinary fields pairs in that case is 12% we cannot overlook this result without further check with higher precision optical observations. In more realistic cases, when we consider the $\Delta\beta$ is more difficult to identify an overshoot, the difference becomes statistical equivalent.

For the $[4'', 6'']$ distanced pairs, we also computed the orientation of galaxies pairs respect the string fields direction, calculating the angle ϕ respect to the Equator. This calculation of the "orientation angle" allowed us to know if the galaxies pairs are oriented orthogonally to the string fields direction as we expect. The result is that the each other's position between the pairs and the fields is almost orthogonal in the sky: this could to suggest that there is the possibility that the galaxies pairs are lensed by a string that should pass in the middle of them.

Even if no definitive conclusion can be draw at this point, there have been intriguing hints of observations that might be signatures of cosmic strings. Further work in the near future should clarify their status, in fact the only "smoking gun" for a CS is the observation of special cuts in outer isophotes of the lensed image. For this purpose, high angular resolution images of the lensed sources are in order. The preliminary results of this study are not conclusive, and further analysis is still required. There are several straightforward improvements one could make to our string searching methods that could improve both the final limits and the searching efficiency in future projects.

This work foresees many possible developments: the next significant advance in this field may be to use higher resolution radio and optical surveys. This improvement can lead to a better analysis in order to prevent the possibility that the signal produced by a real string is diluted by background pairs and to allow the detection of outer faint isophotes of lensed galaxies. In addition, the simple algorithm used in this work can be trasformed in a more sophisticated one, to include constraints on the morphology of galaxies pairs and different values of the separation angle. It is also worth to use the direction of the temperature gradients in radio maps as a criterion in order to exclude those pairs with incompatible orientation. It is appropriate to mention here that there are alternative methods of cosmic string detection that do not require gravitational lensing and analysis of the cosmic microwave background radiation (CMB) data: detection of gravitational wave bursts from the cusps and kinks of cosmic strings.

It is clear, then, that the knowledge about cosmic strings has advanced at a incredible rate over the last 20 years, but there are still many issues to be solved before we can confirm the existence and derive the properties of Cosmic Strings.

Appendix **A**

The area of the surface covering CSc-1

The area covering the CSc-1 consists of 21 overlapping fields. For each field, the coordinates of its four angles are known.

Firstly let us calculate the area of one such field. Secondly we calculate the area of intersection of two neighboring fields (to be excluded from the total area).

Let a surface S be defined by an equation $z = f(x, y)$. The surface S is assumed to be smooth at each point, i.e. there exists a perpendicular to S at each point. Let D be the definition region of the function z on the coordinate plane Oxy (the region D is the projection of the surface S on the plane Oxy). The surface area S which is over the region D is calculated by the formula

$$S = \iint\limits_D \sqrt{1 + \left(\frac{\partial f}{\partial x}\right)^2 + \left(\frac{\partial f}{\partial y}\right)^2} dxdy.$$

Indeed, the angle γ between the perpendicular and the axis Oz is

$$\cos\gamma = \pm\frac{1}{\sqrt{1 + \left(\frac{\partial f}{\partial x}\right)^2 + \left(\frac{\partial f}{\partial y}\right)^2}}.$$

We construct the projection of the unit cell $\Delta\sigma_{ij}$ onto the coordinate plane Oxy:

$$\Delta\sigma_{ij} = \frac{\Delta x_i \cdot \Delta y_i}{\cos\gamma_{ij}},$$

where γ_{ij} is calculated in a point c_{ij}. The complete area of S is limit of the sum:

$$\sum_{i,j} \Delta\sigma_{ij} = \sum_{i,j} \sqrt{1 + \left(\frac{\partial f}{\partial x_i}\right)^2 + \left(\frac{\partial f}{\partial y_j}\right)^2} \Delta x_i \Delta y_j.$$

Finally

$$S = \iint\limits_D \sqrt{1 + \left(\frac{\partial f}{\partial x}\right)^2 + \left(\frac{\partial f}{\partial y}\right)^2} dxdy.$$

Now let z is an implicit function of x and y: $F(x, y, z) = 0$. In that case

$$\frac{\partial F}{\partial x} + \frac{\partial F}{\partial z} \cdot \frac{\partial z}{\partial x} = 0,$$

$$\frac{\partial F}{\partial y} + \frac{\partial F}{\partial z} \cdot \frac{\partial z}{\partial y} = 0.$$

In the implicit case

$$\frac{\partial z}{\partial x} = -\frac{\frac{\partial F}{\partial x}}{\frac{\partial F}{\partial z}},$$

$$\frac{\partial z}{\partial y} = -\frac{\frac{\partial F}{\partial y}}{\frac{\partial F}{\partial z}}.$$

Finally

$$S = \iint\limits_D \frac{\sqrt{\left(\frac{\partial F}{\partial x}\right)^2 + \left(\frac{\partial F}{\partial y}\right)^2 + \left(\frac{\partial F}{\partial z}\right)^2}}{\left|\frac{\partial F}{\partial z}\right|} dxdy.$$

Each field is defined on the sphere $x^2+y^2+z^2 = 1$. For this implicitly defined surface

$$\frac{\partial F}{\partial x} = 2x, \frac{\partial F}{\partial y} = 2y, \frac{\partial F}{\partial z} = 2z,$$

and

$$S = \iint\limits_D \frac{\sqrt{x^2 + y^2 + z^2}}{|z|} dxdy$$

Introducing polar coordinates on the sphere with unit radius

$$x = \cos\alpha, y = \sin\alpha$$

we change cartesian coordinates into polar with jacobian r and obtain

$$S = \int_{r_1}^{r_2}\int_{\alpha_1}^{\alpha_2} \frac{1}{\sqrt{1-r^2}} r d\alpha dr.$$

Let us take as coordinate plane Oxy the plane of the celestial equator. In this case the angle $\alpha \in (0, 2\pi)$ is the right ascension and $\delta \in (0, \pi/2)$ is declination. The axes Oz is directedto the north pole.

The relation between the polar coordinate r and declination angle δ is

$$r_1 = \cos\delta_2, r_2 = \cos\delta_1$$

$$(\delta_1 < \delta_2).$$

For each field $(\alpha_1, \delta_1), (\alpha_2, \delta_2), (\alpha_3, \delta_3), (\alpha_4, \delta_4)$ we take approximately $\alpha_1 = \alpha_3, \alpha_2 = \alpha_4$ and $\delta_1 = \delta_2, \delta_3 = \delta_4$. For example (the field No. 11):

$$\begin{aligned}
&\alpha_1 = 170.56404, \delta_1 = 18.3216;\\
&\alpha_2 = 169.51245, \delta_2 = 18.32824;\\
&\alpha_3 = 170.5539,\ \ \delta_3 = 17.32329;\\
&\alpha_4 = 169.50818, \delta_4 = 17.3299.
\end{aligned}$$

The area

$$\begin{aligned}
S = \int_{\cos\delta_2}^{\cos\delta_1}\int_{\alpha_1}^{\alpha_2} \frac{1}{\sqrt{1-r^2}} r d\alpha dr &= (\alpha_2 - \alpha_1)\cdot(\sin\delta_2 - \sin\delta_1)\\
&\approx (\alpha_2 - \alpha_1)\cdot(\delta_2 - \delta_1)\cdot\cos\frac{\delta_1+\delta_2}{2}
\end{aligned}$$

Since every two fields intersect each other, it is necessary to exclude their intersection area:

$$S_{1,2} = S_1 + S_2 - S_U$$

It's easy to do in terms of projection: we need to arrange the corners of the two intersected fields $\alpha_1^1, \alpha_2^1, \alpha_1^2, \delta_2^2$ and $\delta_1^1, \delta_2^1, \delta_1^2, \delta_2^2$. So, if we have variation row $\tilde{\alpha_1} < \tilde{\alpha_2} < \tilde{\alpha_3} < \tilde{\alpha_4}$ and $\tilde{\delta_1} < \tilde{\delta_2} < \tilde{\delta_3} < \tilde{\delta_4}$ then

$$S_U = (\tilde{\alpha_3} - \tilde{\alpha_2})\cdot(\sin\tilde{\delta_3} - \sin\tilde{\delta_2}) \approx (\tilde{\alpha_3} - \tilde{\alpha_2})\cdot(\tilde{\delta_3} - \tilde{\delta_2})\cdot\cos\frac{\tilde{\delta_3}+\tilde{\delta_2}}{2}.$$

So for fields No. 11 and No. 12 we have

$$\alpha_1^1 = 170.56404, \delta_1^1 = 18.3216;$$

$$\alpha_2^1 = 169.51245, \delta_2^1 = 18.32824;$$
$$\alpha_3^1 = 170.5539, \delta_3^1 = 17.32329;$$
$$\alpha_4^1 = 169.50818, \delta_4^1 = 17.3299.$$

and

$$\alpha_1^2 = 170.37474, \delta_1^2 = 18.66864;$$
$$\alpha_2^2 = 169.32095, \delta_2^2 = 18.67431;$$
$$\alpha_3^2 = 170.36562, \delta_3^2 = 17.67029;$$
$$\alpha_4^2 = 169.31784, \delta_4^2 = 17.67593.$$

For definiteness we choose

$$\alpha_1^1 = 170.56404, \delta_1^1 = 18.3216, \alpha_2^1 = 169.50818, \delta_2^1 = 17.3299$$

and

$$\alpha_2^1 = 170.37474, \delta_2^1 = 18.66864, \alpha_2^2 = 169.31784, \delta_2^2 = 17.67593$$

and arrange the angles

$$(\tilde{\alpha_1}, \tilde{\alpha_2}, \tilde{\alpha_3}, \tilde{\alpha_4}) = (169.31784, 169.50818, 170.37474, 170.56404);$$

and

$$(\tilde{\delta_1}, \tilde{\delta_2}, \tilde{\delta_3}, \tilde{\delta_4}) = (17.3299, 17.67593, 18.3216, 18.66864).$$

The total area for these two intersected fields is.

$$S_{12} = S_1 + S_2 - S_U = 0.99683 + 0.99686 - 0.53213 = 1.46156.$$

It is worth noting that if we sum the single areas of each field, in that calculation we lose the 13% of the total area.

Appendix **B**

Trasformation from the second equatorial system to the galactic system for the string inclination angle

Here we will make the trasformation of the string inclination angle $\beta \in [20^\circ - 30^\circ]$, for which we have an excess of galaxies pairs distances $4'' - 6''$, from the second equatorial system to the galactic system. The transition between the galactic end second equatorial system is written as

$$\sin b = \sin\delta \sin\delta' + \cos\delta \cos\delta' \cos(\alpha - \alpha'),$$

$$\cos b \sin(l' - l) = \cos\delta \sin(\alpha - \alpha'),$$

$$\cos b \cos(l' - l) = \cos\delta' \sin\delta - \sin\delta' \cos\delta \cos(\alpha - \alpha').$$

where (l, b) and (α, δ) are galactic and equatorial coordinates, respectively and (α', δ') are the equatorial coordinates of the galactic pole. In the epoch J1950 (in degree and in radians):

$$\alpha' = 192.25^\circ = 3.355,$$

$$\delta' = 27.4^\circ = 0.478,$$

$$l' = 123^\circ = 2.147.$$

For the optical data, we can estime $\delta \sim \tan\beta \cdot \alpha$, where α changes in the range $[166^\circ, 174^\circ]$ for the thirteen pairs and β is the inclination angle. For the upper limit $\beta = 30^\circ$, we receive

$$b \sim \tan 10^\circ \cdot l$$

and for the lower limit, $\beta = 20°$ we see

$$b \sim \tan 21^0 \cdot l.$$

Therefore, the inclination angle $\beta \in [20°, 30°]$ in second equatorial system became $\beta \in [10°, 21°]$ in galactic system .

Bibliography

[1] Milne, E. A., World-Structure and the Expansion of the Universe. Mit 6 Abbildungen., Zeitschrift für Astrophysik, Vol. 6, p.1 (1933).

[2] Planck 2013 results. XXV. Searches for cosmic strings and other topological defects.,Astron.Astrophys. 571 (2014), arXiv:1303.5085.

[3] A. Achucarro and C. J. A. Martins, arXiv:0811.1277 [astro-ph].

[4]] D. N. Spergel et al. (WMAP), Astrophys. J. Suppl. 170, 377 (2007), astro-ph/0603449.

[5] T.W.B. Kibble. Topology of cosmic domains and strings. J.Phys. A: Math. Gen. V.9, 1976.

[6] Vilenkin A., Shellard E.P., Cosmic strings and other topological defects, Cambridge Univ.Press, UK (1994).

[7] Nielsen, Holger Bech and Olesen, P. (1973). Vortex Line Models for Dual Strings. Nucl.Phys. B61: 45-61.

[8] M.B. Hindmarsh and T.W.B. Kibble. Cosmic strings. Rept.Prog.Phys., 58:477–562, 1995. hepph/ 9411342.

[9] O. S. Sazhina, D. Scognamiglio, M. V. Sazhin Observational constraints on the types of cosmic strings. The European Physical Journal C 74:2972 (2014) arXiv:1312.6106.

[10] E.J. Copeland, T.W.B. Kibble, Cosmic strings and superstrings. Proc. Roy. Soc. Lond. A 466, 623–657 (2010). arXiv:0911.1345v3 [hep-th].

[11] Observational Constraints on Cosmological Superstrings Olga S. Sazhina and Alfiia I. Mukhaeva, Theoretical Physics, Vol. 2, No. 2, June 2017 https://dx.doi.org/10.22606/tp.2017.22003.

[12] J. Polchinski, arXiv:hep-th/0412244; M. Sakellariadou, Phil. Trans. Roy. Soc. Lond. A 366 (2008) 2881 [arXiv:0802.3379 [hep-th]].

[13] T. Vachaspati. Gravitational effects of cosmic strings. Nucl. Phys., B(277):593, (1986).

[14] The Relikt-1 experiment - New results Strukov, I. A.; Brukhanov, A. A.; Skulachev, D. P.; Sazhin, M. V. MNRAS, Vol. 258, Issue 1 (1992), Pages 37P–40P.

[15] A. Vilenkin. Looking for cosmic strings. Nature, 322:14, (1986).

[16] O.S. Sazhina, The study of dark energy by the methods of astronomy., (2012).

[17] http://www.sdss.org/dr12/scope/.

[18] Mikhail V. Sazhin, Olga S. Sazhina, Massimo Capaccioli et al., Gravitational Lens Images Generated by Cosmic Strings, The Open Astronomy Journal, (2010), 3, 200-206.

[19] Sazhin M.V., Capaccioli M., Longo G., Paolillo M., Khovanskaya O.S., Further spectroscopic observations of the CSL-1 object, Astrophys.J. 636 (2005) L5-L8.

[20] Sazhin M.V., Khovanskaya O.S., et al., Gravitational lensing by cosmic strings: What we learn from the CSL-1 case, MNRAS 376 (2007) 1731.

[21] D. Garfinkle, General relativistic strings, Phys. Rev. D 32, 1323, (1985).

[22] Zakharov A. F., Sazhin M. V. Gravitational microlensing. Phys.Usp.41 945-982, (1998).

[23] The Sloan Digital Sky Survey SkyServer DR12, http://skyserver.sdss.org/dr12/en/tools/chart/navi.aspx.

[24] The STScI Digitized Sky Survey, http://archive.stsci.edu.

[25] Reid I.N., Brewer C., Brucato R.J., et al., (1991), PASP 103, 661.

[26] Kibble T.W.B., Topology of cosmic domains and strings, J.Phys.A:Math.Gen., (1976).

[27] Sazhin M.V., et al., CSL-1: chance projection effect or serendipitous discovery of a gravitational lens induced by a cosmic string?, MNRAS 343 2 (2003) 353.

[28] J.M. Alcalà, M. Pannella, E. Puddu, M. Radovich, R. Silvotti, A. Arnaboldi, M. Capaccioli, et al. The capodimonte deep field i - presentation of the survey and first follow-up studies. Astron. and Astrophys., 428:339–352, (2004).

[29] M.V. Sazhin, O. Khovanskaya, M. Capaccioli, G. Longo, J.M. Alcalà, R. Silvotti, and M. Pavlov. Search for gravitational lenses near the extragalactic double object csl-1. Astronomy Letters, 31(2):73–79, (2005). astro-ph/0406516.

[30] M.V. Sazhin, O. Khovanskaya, M. Capaccioli, G. Longo, M. Paolillo, G. Covone, N.A. Grogin, and E.J. Schreier. Gravitational lensing by cosmic string: what we learn from the csl-1 case. Mon. Not. Royal Astr. Soc., 376:1731–1739, (2007). astro-ph/0611744.

[31] N. Kaiser and A. Stebbins. Microwave anisotropy due to cosmic strings. Nature, 310:391, (1984).

[32] Fixsen DJ, Cheng ES, Gales JM, Mather JC, Shafer RA, et al. (1996). Ap. J. 473:576–587

[33] U.-L. Pen, U. Seljak, N. Turok, Power spectra in global defect theories of cosmic structure formation. Phys. Rev. Lett. 79, 1611– 1614 (1997). arXiv:astro-ph/9704165.

[34] R. Battye, A. Moss, Updated constraints on the cosmic string tension., Phys. Rev. D 82, 023521 (2010), arXiv:1005.0479.

[35] M.B. Hindmarsh. The Formation and evolution of cosmic strings, chapter Seaching for Cosmic Strings, page 527. Cambridge Univ. Press, (1990).

[36] O.S. Sazhina, M.V. Sazhin, V.N. Sementsov, Anisotropy of CMBR induced by a straight moving cosmic string (in Russian). JETP 133(5), 1005, (2008).

[37] O.S. Sazhina, V.N. Sementsov, N.T. Ashimbaeva, Cosmic string detection in radio surveys. Astron. Rep. 58(1), 16–29, (2014).

[38] E. Jeong and G.F. Smoot. The validity of the cosmic string pattern search with the cosmic microwave background. ApJL, 661, (2007).

[39] N. Kaiser, A. Stebbins, Microwave anisotropy due to cosmic strings. Nature 310, 391–393, (1984).